

**A Study of the Luminosity and Mass Functions of the Young IC 348 Cluster  
using FLAMINGOS Wide-Field Near-Infrared Images**

A. A. Muench<sup>1,4,5</sup>, E. A. Lada<sup>1,4</sup>, C. J. Lada<sup>2,4</sup>, R. J. Elston<sup>1,4</sup>, J. F. Alves<sup>3,4</sup>,  
M. Horrobin<sup>1,4</sup>, T. H. Huard<sup>2,4</sup>, J. L. Levine<sup>1,4</sup>, S. N. Raines<sup>1,4</sup>, and C. Roman-Zuniga<sup>1,4</sup>,

**ABSTRACT**

We present wide-field near-infrared (*JHK*) images of the young,  $\tau = 2$  Myr IC 348 cluster taken with FLAMINGOS. We use these new data to construct an infrared census of sources, which is sensitive enough to detect a  $10 M_{Jup}$  brown dwarf seen through an extinction of  $A_V \sim 7$ . We examine the cluster's structure and relationship to the molecular cloud and construct the cluster's *K* band luminosity function. Using our model luminosity function algorithm we derive the cluster's initial mass function throughout the stellar and substellar regimes and find that the IC 348 IMF is very similar to that found for the Trapezium Cluster with both cluster IMFs having a mode between  $0.2 - 0.08 M_{\odot}$ . In particular we find that, similar to our results for the Trapezium, brown dwarfs constitute only 1 in 4 of the sources in the IC 348 cluster. We show that a modest secondary peak forms in the substellar IC 348 KLF, corresponding to the same mass range responsible for a similar KLF peak found in the Trapezium. We interpret this KLF peak as either evidence for a corresponding secondary IMF peak at the deuterium burning limit, or as arising from a feature in the substellar mass-luminosity relation that is not predicted by current theoretical models. Lastly, we find that IC 348 displays radial variations of its sub-solar ( $0.5 - 0.08 M_{\odot}$ ) IMF on a parsec scale. Whatever mechanism that is breaking the universality of the IMF on small spatial scales in IC 348 does not appear to be acting upon the brown dwarf population, whose relative size does not vary with distance from the cluster center.

*Subject headings:* infrared: stars — open clusters and associations: individual (IC 348) — stars: luminosity function, mass function — stars: low-mass, brown dwarfs — stars: formation

---

<sup>1</sup>Department of Astronomy, University of Florida, Gainesville, FL 32611

<sup>2</sup>Harvard-Smithsonian Center for Astrophysics, Cambridge, MA 02138

<sup>3</sup>European Southern Observatory, Karl-Schwarzschild-Strasse 2, 8574 Garching Germany

<sup>4</sup>Visiting Astronomer, Kitt Peak National Observatory. KPNO is operated by AURA, Inc. under contract to the National Science Foundation.

<sup>5</sup>present address: SIRTf Science Center, California Institute of Technology, Pasadena, CA 91125 USA

## 1. Introduction

For the past few decades, advances in near-infrared (NIR) detector technology have provided new and exciting discoveries of young clusters and star forming regions. For example, the partially embedded cluster IC 348, which is the focus of this paper, was first observed in the infrared using a single channel photometer (Strom et al. 1974). However, such early observations were severely limited in both sensitivity and angular resolution, allowing for the detection of only the brightest embedded cluster members. For example, Strom et al. observed 25 possible stellar members of the IC 348 cluster with  $K \leq 10.5$  while discovering a few bright but heavily embedded IR sources.

The development of NIR infrared imaging arrays  $\sim 15$  years ago, greatly enhanced our ability to study young clusters by not only improving the sensitivity and angular resolution of NIR studies but also the areal coverage. For the first time, large scale ( $\sim$  square degree) surveys of molecular clouds (e.g., Orion B GMC; Lada et al. 1991) and in particular of young clusters such as IC 348 (Lada & Lada 1995) were conducted. Such surveys revealed the presence of hundreds of young stars over a wide mass range contained within the young clusters, increasing the number of stellar sources in IC348 by a factor of 15 and increasing the depth by a factor of 40 over earlier studies. While these early NIR imaging surveys were clearly a vast improvement over surveys that had used single channel photometers, they were not without their limitations. In particular they required obtaining large mosaics containing tens to thousands of individual frames per wavelength band to cover the desired star forming area. For example Lada & Lada obtained twenty four separate fields to cover the central parsec of IC 348. Consequently there was often a trade off between survey depth and area covered and, therefore in the case of many young clusters, obtaining a complete census of its members was still unattainable.

The most recent advancements in NIR detector technology have permitted the development of sensitive, wide-field infrared cameras such as FLAMINGOS (Elston 1998, Elston et al. 2003, in preparation), allowing more than an order of magnitude improvement in areal coverage and depth. In terms of young cluster studies, these improvements now enable us to obtain a complete census of stars of all masses, even deeply embedded ( $A_V \sim 5 - 10$ ) young brown dwarfs with masses as small as 10 Jupiter masses, over the complete spatial extent of the cluster. Observing the full angular extent of young clusters may be critical for obtaining a complete stellar census since recent theoretical studies show that mass segregation (primordial or dynamical) may be present in even the youngest embedded clusters (Bonnell, Bate, Clarke, & Pringle 2001; Kroupa, Aarseth & Hurley 2000). Thus, for the first time we are poised to study the complete populations of young star clusters to below the hydrogen burning limit rather than focusing only on the stellar population of only the clusters' cores.

Since the Lada & Lada NIR survey, IC 348 has been the target of a number of wide-field optical (Luhman 1999),  $H\alpha$  (Herbig 1998) and X-ray imaging (Preiblich, Zinnecker & Herbig 1996) studies, and all have reinforced the ideas that IC 348 is partially embedded at the edge of the Perseus GMC and IC 348 is spatially extended on the sky beyond its central core (Lada & Lada 1995). With our current wide-field NIR image we are able to survey an area encompassing nearly all the boundaries of these past surveys while simultaneously extending the Lada & Lada NIR survey depth by nearly 3 magnitudes. Thus, we are

able to detect very low mass sources ( $0.01M_{\odot}$ ) over a much larger cluster volume (larger extinction) than any prior survey. We use the results of our infrared census to examine the cluster’s structure, reddening and relationship to the Perseus Molecular Cloud (Section 2) and construct the cluster’s differential  $K$  band luminosity function (Section 3). In Section 4 we combine our deep survey, a spectroscopically determined age estimate for IC 348 from Herbig (1998) data, and our improved luminosity function modeling techniques (Muench et al. 2002, hereafter, Paper I) to derive the IMF of IC 348 across the stellar and sub-stellar regimes. Lada & Lada (1995) found that the turnover in the IC 348 KLF can be modeled by a similar peak and turnover in the underlying IMF; we expand on their finding by showing that the composite cluster IMF forms a mode near  $0.1 M_{\odot}$ , turns over and declines throughout the brown dwarf regime down to near  $30M_{Jup}$ . Our wide-field imaging also allows us to derive the cluster’s stellar and sub-stellar IMF over a much larger area than similarly sensitive surveys, which have concentrated on the cluster’s central core (Luhman et al. 1998; Najita, Tiede, & Carr 2000, hereafter, NTC00). From this analysis, we compare our results for IC 348 and the Trapezium (Paper I) and discuss in Section 5 the impact of spatial or statistical IMF variations on meaningful comparisons of the IMFs for different clusters.

## 2. Wide-Field Near-Infrared Images of IC 348

### 2.1. FLAMINGOS Observations

We obtained wide-field near-infrared images of the IC 348 cluster using the FLoridA Multi-object Imaging Near-IR Grism Observational Spectrometer (FLAMINGOS, Elston 1998) on the 2.1m telescope at the Kitt Peak National Observatory, Arizona (USA) during December 2001 and February 2002. The FLAMINGOS instrument employs a 2K HgCdTe “HAWAII-2” imaging array, which when configured on the 2.1m Kitt Peak telescope yields a  $20.5' \times 20.5'$  field of view with a derived plate scale at  $K$  band of  $\sim 0.608''/\text{pixel}$ .

On both 14 December 2001 and 08 February 2002 dithered sets of IC 348 images were obtained with FLAMINGOS in the  $J$  ( $1.25 \mu\text{m}$ ), the  $H$  ( $1.65 \mu\text{m}$ ) and the  $K$  ( $2.2 \mu\text{m}$ ) (or  $K_s$  --  $2.162 \mu\text{m}$ ) bandpass. These image sets were obtained within a narrow window of time (1.5 - 2.5 hrs) and a restricted range of airmass ( $\text{sec } z < 1.4$ ). We list the details of these observations in Table 1. Briefly, we employed a large number (15-50) of short (20-60 sec) non-repeating dithers to yield total integration times of approximately 14-24 minutes, depending upon the bandpass. Conditions on both nights appeared photometric, with no apparent cloud cover, stable background sky counts, and seeing estimates between  $1.6 - 1.9''$  on 14 December 2001 and  $1.5 - 1.7''$  on 08 February 2002.

Two wide-field off-cluster images were similarly imaged in the  $K$  or  $K_s$  bands on 17 December 2001 and 11 February 2002. These two non-overlapping regions lie approximately 1 degree east of IC 348, along a line of constant galactic latitude with the young cluster. Their equatorial field centers were: 1)  $03^{\text{h}}48^{\text{m}}21^{\text{s}}.9$ ;  $+31^{\circ}38'06''.7$  (J2000); and 2)  $03^{\text{h}}48^{\text{m}}19^{\text{s}}.4$ ;  $+31^{\circ}08'34''.7$  (J2000). Additional details of these off-field observations are also listed in Table 1.

We reduced the sets of dithered frames with the April 2002 version of the FLAMINGOS data reduction pipeline (Elston et al 2003, in preparation). Local sky flat-fields were used for  $J$  and  $H$  bands, while dome flats were used for  $K$  or  $K_s$  bandpass. Briefly, the FLAMINGOS data reduction pipeline is based upon a two-pass routine with object masking during the second pass that permits the creation of star-free median sky frames from the target images while following standard techniques for the reduction of near-infrared data. To take advantage of the relatively large number of dithers in our datasets, the pipeline employs the drizzle IRAF routine (Fruchter & Hook 2002) to allow for linear sub-pixel image reconstruction during the final combination of the dithered frames. In summary, 6 reduced cluster images (2 at each bandpass) were obtained, in addition to two  $K$  band off-field images.

In Figure 1 we display a (false) color composite, near-infrared image of IC 348 using the  $J$ ,  $H$ , and  $K_s$  FLAMINGOS images from our February 2002 observations. A number of interesting cluster features are outlined by low-level nebulosity. These include the cluster core, which displays deep red nebulosity suggestive of somewhat higher extinction, and the interface between the IC 348 cluster and the molecular cloud all along the southern edge of the image. This interface region includes numerous signposts of very recent star formation including the HH-211 infrared jet (McCaughrean, Rayner, & Zinnecker 1994), the enshrouded NIR source deemed the “Flying Ghost” nebula (Strom et al. 1974; Boulard et al. 1995), a dark lane suggestive of a flared, edge-on disk-like structure, and a number of bright infrared sources detected only in the  $K$  band.

A few image artifacts can also be seen in this figure. These include geometric distortions of the stars in the northeast corner of the image, red and green glint features due to internal reflections along the southern edge of the cluster, and coma-like ghosts south-southwest of the cluster center, resulting from a long time constant in one amplifier of the HAWAII-2 array. On the other hand, the alternating blue-green-red source located south-southwest of the cluster center is not an image artifact, but instead is the asteroid 545 Messalina.

## 2.2. The Infrared Census

### 2.2.1. Photometry and Calibration

We characterized each reduced image by deriving estimates of the FWHM of the stellar point spread function and the pixel-to-pixel noise in the background sky using the IMEXAMINE IRAF routine, although the pixel-to-pixel noise is correlated in drizzled images. The resulting seeing estimates and  $5\sigma$  detection limits are listed in Table 1. We find that the slightly better seeing and longer exposure times of the February data yielded detection limits approximately 1 magnitude fainter than the December observations. Sources were initially identified on each reduced image using the stand-alone S-Extractor package (Bertin & Arnouts 1996). In an iterative fashion, accurate centroids were calculated for the detected sources using the CENTER IRAF routine, and marked on the reduced images, after which the images were manually searched to identify false detections or to add sources missed near bright stars. The source lists for each of the 6 on-cluster images were then cross-correlated to identify and check those sources not appearing on all the images.

Multi-aperture photometry was performed on the sources using the APPHOT IRAF package and the instrumental magnitudes were corrected out to the beginning of the sky annulus using photometric curves of growth calculated from  $\sim 20$ – $30$  bright stars using the MKAPFILE IRAF routine. From the corrected multi-aperture photometry, we chose to use the smallest beamsize that simultaneously gave the most consistent photometry when compared to larger apertures. Because of a spatially varying PSF due to geometric distortions present in the final images, we resorted to using a rather large aperture (radius = 5 pixels; beam-size =  $6''$ ), yielding aperture corrections typically of order  $\lesssim 0.06$  magnitudes. Absolute calibration of the instrumental photometry was performed using zeropoint and airmass corrections derived from Persson et al. (1998) standard stars, which were observed on the same night as the targets. For secondary calibration, we calculated and removed median zeropoint offsets of order  $\sim 0.04$ – $0.08$  magnitudes between our absolute photometry and the 2MASS photometric system. Because the natural system of our photometry is not known, the observed colors of our sources have not been transformed to the 2MASS system. Complete source lists for the FLAMINGOS IC 348 cluster observations presented in this paper, including equatorial positions and aperture photometry from the December 2001 and February 2002 datasets, will be made available electronically at the FLAMINGOS website at the University of Florida <sup>6</sup>. Final products of the associated NOAO Survey project, “Toward a Complete Near-Infrared Spectroscopic and Imaging Survey of Giant Molecular Clouds,” will be made available through the NOAO Science Archive <sup>7</sup>.

### 2.2.2. Accuracy

We quantified our photometric accuracy by directly comparing the photometry from the December and February images and by matching our data to the 2MASS catalog. We list the results of our photometric comparison to 2MASS in Table 2. This table includes the magnitude range of the comparisons based on the FLAMINGOS saturation and 2MASS photometric limits, the secondary calibration offsets applied in Section 2.2.1, and the  $1\sigma$  dispersion between the datasets.

While the 17 December off-field data display a dispersion of  $\sim 3\%$  at K band relative to the 2MASS catalog, we found *JHK* dispersions in the 14 December on-cluster data that were larger than expected from purely photometric errors with the *K* band scatter 4% larger in the on-cluster frame than that found in the off-cluster frame taken three days later under similar sky conditions. We attribute some of this additional scatter to the intrinsic variability of young PMS stars in IC 348 (Herbst, Maley & Williams 2000), which in the infrared typically peaks at *J* band (Carpenter, Hillenbrand & Strutskie 2001) (i.e., for our IC 348 data  $\sigma_K = 0.05$  versus  $\sigma_J \sim 0.07$  mag).

Between 03 - 11 February 2002, oil from the primary mirror cell contaminated the FLAMINGOS dewar window. This contamination had a negligible effect on our *J* and *H* band photometry since these data were flat-fielded with local, contemporaneous sky flats. However, the *K* data were flat-fielded using

---

<sup>6</sup><http://www.flamingos.astro.ufl.edu/>

<sup>7</sup><http://archive.noao.edu/nsa/>

non-contemporaneous dome flat-fields and display a 4–6% increase in the photometric scatter relative to the FLAMINGOS data obtained in December and to the 2MASS catalog. This scatter does not affect the analysis or conclusions of this paper.

### 2.2.3. Results

After considering the different saturation, detection and noise limits of the December and February IC 348 FLAMINGOS data, we produced a single working source list with photometry drawn from both FLAMINGOS datasets. We chose to use the December  $K$  band data down to  $m_K \sim 15.5$ . Below this value we transitioned to the intrinsically deeper February  $K_s$  data. In the  $J$  and  $H$  bands we averaged the two datasets between the saturation and the detection limits of these respective catalogs, recording the  $1\sigma$  standard deviation between the two observations. For the brightest 39 stars, which were saturated in one or more bands on all of our images, we substituted the 2MASS photometry for our FLAMINGOS photometry. Finally, for the faintest objects ( $m_J > 18.5$ ;  $m_H > 17.5$ ;  $m_K > 17.0$ ) we used smaller aperture photometry (radius = 3.5 pixels, aperture correction =  $\sim -0.12$  mag).

In Figure 2 we present the infrared color-magnitude diagrams ( $J-H$  vs  $H$  and  $H-K$  vs  $K$ ) for the FLAMINGOS IC 348 region without filtering for photometric error. We compare the distribution of sources in these diagrams to the location of pre-main sequence isochrones taken from the D’Antona & Mazzitelli (1997) and Baraffe et al. (1998) evolutionary models. For these comparisons we assume a cluster mean age of 2 Myr and a distance of 320 pc (see Sections 4.1 and 4.2 for further discussion of these parameters). For these cluster parameters we find that we are sensitive to a 2 Myr,  $80M_{Jup}$  object at the hydrogen burning limit seen through  $\sim 30$  magnitudes of extinction or a  $10M_{Jup}$  brown dwarf near the deuterium burning limit seen at an  $A_V = 7$  (using the Burrows et al. 1997, theoretical models). Three general characteristics of the sources projected towards our IC 348 FLAMINGOS region are clearly seen: 1) The color-magnitude diagrams indicate a cluster region having only modest reddenings relative to other star forming regions, with the vast majority of the sources having  $A_V < 7$ ; 2) There is a density of sources between  $10 < m_K = m_H < 15$  that is closely outlined by the PMS isochrones and represents a range of magnitude space that appears dominated by likely cluster members; 3) Below  $m_K = m_H = 15$  the color-magnitude distribution appears to become dominated by field-stars (and likely galaxies) as indicated by a rapid increase and steady broadening in the density of sources on these plots. All of these features were seen in individual datasets (December vs February) and were not modified if we changed any of the parameters for merging the data (e.g., the use of  $K$  instead of  $K_s$  data for the faintest objects).

In Figure 3, we display the infrared  $H-K$  vs  $J-H$  color-color diagram for sources in the IC 348 region. We include sources most likely to be cluster members by using characteristics (2) and (3) of the color-magnitude diagrams listed above to apply a somewhat arbitrary  $m_K = 15$  magnitude limit. The “cluster sample” resulting from this magnitude cut should be complete for unreddened 2 Myr brown dwarfs down to  $0.025M_\odot$  ( $\sim 25M_{Jup}$ ) and for  $0.04M_\odot$  ( $\sim 40M_{Jup}$ ) brown dwarfs seen through  $A_V \sim 7$ .

There are 580 sources with  $m_K < 15$  of which 563 have  $JHK$  photometry; we display all of these in the

color-color diagram without filtering for error. Again, it is clear that the cluster region is only marginally reddened with the nearly all of the sources having  $A_V < 7$ . The overwhelming majority of the sources fall within a locus bounded by the reddening vectors for the giant branch and the tip of the M dwarf sequence. While one source has NIR colors significantly to the left of the reddening band, 66 sources have infrared colors which lie to the right of the reddening vector for M9 dwarfs ( $H - K_s = 0.46$ ; Kirkpatrick et al. 2000). These sources fall into a region of infrared excess in the color-color diagram, which because IC 348 is a very young cluster are considered to be likely cluster members with optically thick, circumstellar disks. Finally, 42 of these sources exhibit infrared excesses greater than their  $1\sigma$  photometric noise, and we note that these filtered sources span the entire range of H band magnitude both above and below the expected luminosity of the hydrogen burning limit. With these basic observational results we examined the structure of the IC 348 cluster.

### 2.3. Cluster Structure

For our subsequent analysis of the luminosity and mass function of IC 348 we wished to select that portion of the FLAMINGOS wide-field image that provides the best sampling of the overall cluster. Studying a region somewhat similar in size to the FLAMINGOS area, Lada & Lada (1995) used a surface density analysis to show that IC 348 could be broken into 9 apparent sub-clusterings spread across their survey region. Although subsequent wide-field  $H\alpha$  (Herbig 1998) and optical (Luhman 1999) surveys covered areas similar to LL95, most studies of the IMF of IC 348 have concentrated on the central LL95 sub-cluster, IC348a (Herbig 1998; Luhman et al. 1998, ; NTC00) and have not included the other LL95 sub-clusters. While existing optical and  $H\alpha$  studies may systematically underestimate the cluster size due to extinction or miss members that do not display  $H\alpha$  emission, they have confirmed that the cluster is in fact spread over an area larger than the IC348a region. Using the deeper wide-field near-infrared imaging provided by our FLAMINGOS observations, we re-investigated the structure of the IC 348 cluster by calculating the cluster’s radial profile and by examining the spatial distribution of sources.

#### 2.3.1. Cluster Radius

In Figure 4 we construct the radial profile of sources in the FLAMINGOS IC 348 region, centering on the IC 348a sub-cluster. We use only those sources for which  $m_K < 15$  and calculate the surface density in stars per square degree using both annuli of equal width and annuli having constant areas. We compare the resulting radial profiles to the field star surface density calculated from our off-field data. Clearly the cluster exceeds the unreddened background surface density over most of the FLAMINGOS region. Specifically, the cluster extends over an area considerably larger than the IC348a sub-cluster, whose radius was given as 0.47 pc ( $5.05'$ ) in LL95 and over an area larger than the radius of  $4'$  calculated by Herbig. The cluster appears to dip to the unreddened background surface density at a radius of  $\sim 10 - 11'$ ; however, since this radius is also where the profile begins to clip the edge of the survey region, we cannot confidently rule out a larger cluster radius using the current FLAMINGOS image. At the distance of IC 348, this translates to a

cluster radius of  $\sim 1$  pc, similar to the effective radius of 1.19 pc derived by Carpenter (2000).

To provide a means for comparing our study to that of other authors, we separated our FLAMINGOS cluster region into two sub-divisions based upon the radial profile and assigned these two sub-regions primarily functional names, e.g., the cluster “core” sub-region with a radius =  $5'$  and the cluster “halo” region between the cluster “core” and a radius of  $10.33'$ , corresponding to the largest unclipped radius permitted by the current FLAMINGOS survey. The core region approximately represents the IC 348a sub-cluster but is slightly larger than that area studied by Luhman et al. (1998) and NTC00, while the halo region covers an area approximately 3.3 times that of the core and encompasses the stars contained in the sub-clusters designated *b-i* by LL95. Naturally, we are viewing a three-dimensional cluster in projection, such that true “halo” sources will also be present in the cluster’s “core” sub-region, and therefore will somewhat blur the meaning of our division of the cluster by area.

Although our construction of the cluster’s radial profile allowed us to divide the spatial extent of IC 348 within our survey region, we found that it follows neither a simple  $r^{-1}$  nor a King profile. We fit both analytical profiles to the cluster’s constant area annuli profile, varying the radial extent of the fits, and for the King profile, allowing both the core and tidal radii to vary freely. Neither analytic profile provided reasonable  $\chi^2$  fits to the entire cluster profile. As we display in Figure 4, the tail of the cluster profile, (i.e., the halo sub-region), is much flatter than either of the analytic profiles, and this is likely the reason Herbig derived a smaller cluster radius. One interpretation of these fits is that the LL95 sub-clusters, which constitute the cluster’s halo, are actually separate entities, rather than being statistical fluctuations on a  $r^{-1}$  cluster profile.

Our construction of the IC 348 radial profile and the subsequent analytical fits likely suffer from two problems. First, we use circular annuli, while, as we will show in Figure 5b, the cluster is elliptically elongated in the N-S direction. Second, we rely upon an empirical estimate of the field-star surface density from a region near to IC 348 but that, in principle, could fluctuate between this location and the background relevant to IC 348. Indeed, the surface densities of the two off-cluster locations fluctuate more than expected purely from counting statistics despite their similar galactic latitudes. This spatial fluctuation, however, is exceedingly small relative to the excess surface density of the cluster halo and will not likely affect the cluster boundary we derive. On the other hand, the obscuration of background field stars by the parental molecular cloud will lower the expected field star surface density and will affect the derived cluster radius, as we illustrate in Figure 4. Reddening the background by the average extinction in the IC 348 region ( $A_V = 4$ ; see Section 2.4) only expands the cluster radius by  $1-2'$ , however, and the cluster probably does not exceed a radius of  $15'$  (1.4pc), which is a boundary traced very clearly by wide-field X-ray detections (Preiblich, Zinnecker & Herbig 1996).

### 2.3.2. *Spatial Distribution of Sources*

With the purpose of characterizing our two cluster sub-regions, we examined the spatial distribution of the IC 348 FLAMINGOS sources, plotting them using separate symbols for different luminosity ranges in

Figure 5a.

By segregating the two sub-regions, we find, for example, that there are as many relatively bright sources  $m_K < 10$  (i.e., with  $\gtrsim 1 M_\odot$ ) in the cluster core as in the cluster halo. Since there are only a handful of early (B or A) type stars in IC 348, there is no statistically meaningful way to show that the 3 BA stars in the cluster core are “segregated” relative to the 2 A stars and the B0III star  $\alpha$  Persei in the cluster halo. On the other hand, the faintest sources ( $m_K > 15$ ) do show some spatial variations, with a sharp decrease in these sources along the cluster’s southern edge, outlining the interface of the cluster with the molecular cloud.

In Figure 5b, we display a surface density plot of IC 348 from the 580 sources with  $m_K < 15$  used to construct the cluster’s radial profile (see Figure 4) and smoothed with a box filter at the Nyquist sampling. The box filter had a width of  $200''$  or an area roughly equivalent to the area of the annuli used in the radial profile. At this resolution, only a smooth N-S elongated cluster is seen with no significant sub-clusterings. We confirmed, however, that if we use the same spatial resolution as the Lada & Lada study ( $90''$ ), we recovered most of the sub-clusters identified by LL95 and that now lie in the cluster’s halo. Further, these surface density contour maps display no apparent correlation to the location of the cluster-cloud interface region at either resolution.

Lastly, we examined the locations of the 66 sources displaying NIR excess. As was found by LL95, the majority of these sources lie outside of the cluster core. Moreover, the surface density of these NIR excess sources appears to increase toward the southern interface with the Perseus Molecular Cloud, opposite to the trend in the distribution of the faintest objects. These patterns suggest that many of the NIR excess sources are correlated to and likely embedded within the molecular cloud, and may be associated with the most recent star formation events in the IC 348 region.

## 2.4. Cluster Reddening Properties

We also used the sources observed within the IC 348 region as line of sight probes of the parental molecular cloud, allowing us to characterize the reddening that would be seen towards cluster members or background field-stars. Building upon methods developed in Lada, Lada, Clemens, & Bally (1994) and Alves et al. (1998) and our recipe(s) described in Muench et al. (2002), we calculated individual extinction estimates for each source by de-reddening the sources’ infrared colors to a locus of assumed intrinsic colors in the  $(H-K)$  vs  $(J-H)$  color-color diagram. These extinction estimates were used to create reddening maps of the cluster region and show that IC 348 is primarily foreground of the remnant molecular material. Further, we binned these individual  $A_V$  estimates into extinction probability distribution functions (hereafter known as EPDFs), which we will use when estimating the number of interloping field-stars and when calculating luminosity function models to interpret the observations.

#### 2.4.1. Extinction Estimates and Reddening Maps

We calculated individual  $A_V$  for sources falling into two different luminosity ranges, dividing them into sets that are likely dominated by either cluster members or background field-stars. We separated the “bright – cluster” and “faint – background” samples based upon their location in the  $(H - K)$  vs  $K$  color-magnitude diagram relative to the reddening vector of a source at  $m_K = 15$  ( $H - K = 0.35$ ). The “faint” sample was also limited to objects brighter than a reddening vector for a source at  $m_K = 17$ , ( $H - K = 0.4$ ).

The two magnitude samples were de-reddened back to different loci of assumed intrinsic colors. The “bright” sources were assumed to be young PMS stars with masses as small as  $\sim 0.03 M_\odot$ . 95% of these have  $JHK$  colors and were de-reddened back to the classical T-Tauri Star (cTTS) locus in the  $JHK$  color-color diagram (Meyer, Calvet & Hillenbrand 1997, slope = 0.58;  $J - H$  intercept = 0.52), while the remaining 5% were assigned an intrinsic  $H - K$  color = 0.5 and  $A_V$  estimates derived. The “faint” sources were assumed to be dominated by field M dwarfs and those with  $JHK$  colors ( $\sim 85\%$ ) were de-reddened back to a linear approximation of the M dwarf branch in the color-color diagram (from K6 to M9, slope = 0.16;  $J - H$  intercept = 0.61)<sup>8</sup>, while the remaining 15% lacking  $J$  band were assigned an intrinsic  $H - K = 0.16$ .

In Figure 6 we present the resulting extinction maps derived from these two samples. Both maps clearly define the location of the cluster-cloud interface along the region’s southern border, while they also outline a NE-SW band of reddening that passes through the cluster’s core, similar to the cluster’s N-S elongation. One straightforward conclusion from the spatial variations in either reddening map is that the IC 348 region cannot be characterized by a single mean  $A_V$  value. Although the two  $A_V$  maps are physically very similar, the reddening seen by the background stars is in general larger than that foreground to the cluster members, indicating that the remnant molecular cloud lies primarily behind the cluster core rather than in front of it.

#### 2.4.2. Extinction Probability Distribution Functions (EPDFs)

In Figure 7 we plot the normalized histograms of the  $(H - K)$  color and of  $A_V$  for sources in the two magnitude ranges defined in the previous section and separate them further by cluster sub-region. As expected from the  $A_V$  maps, the faint sources’ color and  $A_V$  distributions are broader and redder than the bright, likely cluster stars, although the EPDFs of the likely cluster members in both regions appear somewhat similar. Applying a two-sided Kolmogorov-Smirnov test to the  $A_V$  values derived from bright and faint sources in the cluster core, we found that it is unlikely that they are drawn from the same  $A_V$  distribution, having a KS probability of only 0.00024. This is in contrast to the halo sub-region, where the bright and faint stars have a 0.23 probability of being drawn from the same  $A_V$  distribution. Similarly the bright stars in the core and halo have a 0.043 probability of being drawn from the same distribution while the faint stars in both regions cannot, ruled out at the  $2.0000 \times 10^{-8}$  confidence. Taken together, the EPDFs and these statistical tests support two basic conclusions about the reddening seen towards IC 348: 1) there is a

---

<sup>8</sup>These cTTS and M dwarf approximations result in nearly all field giants being de-reddened to the colors of the K1 - K2III spectral class.

measurable difference in the reddening seen by the background stars between the core and halo sub-regions, owing to the cluster lying in front of substantial molecular material (also see Figure 6b); 2) the bright, likely cluster members of the core and halo appear to have fairly similar reddenings, despite the projection of the entire region onto various pieces of the Perseus GMC.

The normalized  $A_V$  histograms (i.e., EPDFs) are generally skewed to  $A_V < 5$  and are quite non-gaussian, again indicating that a single  $\langle A_V \rangle$  value is inappropriate to describe the cluster reddening. On average we find reddenings to the background stars of  $\langle A_V \rangle_{core} \sim 7.2$  ( $1\sigma = 6.3$ , avg. deviation = 4.6, median = 5.3) and  $\langle A_V \rangle_{halo} \sim 4.6$  ( $1\sigma = 4.3$ , avg. deviation = 3.0, median = 3.4), while to the likely cluster members these averages are  $\langle A_V \rangle_{core} \sim 4.9$  ( $1\sigma = 4.2$ , avg. deviation = 2.9, median = 3.8) and  $\langle A_V \rangle_{halo} \sim 4.2$  ( $1\sigma = 4.0$ , avg. deviation = 2.6, median = 3.3). These latter averages are roughly the same as the  $A_K \sim 0.5$  assumed by LL95 for the entire IC 348 region. More meaningful comparisons can be made to those studies that have used spectroscopic observations to derive individual  $A_V$  estimates. Our  $\langle A_V \rangle$  estimates are consistent with the  $\langle A_V \rangle = 2.8$  derived by Herbig over a large cluster area. In the core, we compared our  $A_V$  estimates to the  $A_K$  estimates derived in NTC00 using spectral types that were derived from narrowband imaging, and which was in principle deep enough to probe the extinction seen to background stars. From 106 matched sources<sup>9</sup> with non-zero extinction estimates in both catalogs, we find that they are fairly similar, with  $\langle A_K \rangle_{NTC00} = 0.47(0.38)$  compared to  $\langle A_K \rangle = 0.35(0.26)$  for our work. Direct comparison of the EPDFs constructed from these two studies confirmed that they appear consistent with the NTC00 EPDF being somewhat broader. The effective difference, ( $\delta A_K \sim 0.1$  between the  $\langle A_K \rangle$ ), between these EPDFs is much smaller than the bins of the  $K$  band luminosity functions we are employing in our subsequent mass function analysis. Thus, it should not affect our derivation of and overall conclusions about the IMF of IC 348. On the other hand, it may bring added uncertainty to our statistical census of very low mass brown dwarfs ( $M < 0.02M_\odot$ ; see also Section 5.1.2). Since our study is better sampled (using more stars) and probes a much larger volume of the cluster region than prior studies, we used the EPDFs derived here when correcting for background field-stars (Section 3.2) and when modeling of the cluster’s luminosity function (Section 4.4).

### 3. The Infrared Luminosity Functions of IC 348

#### 3.1. Constructing Infrared Luminosity Functions

We constructed the raw infrared ( $JHK$ ) luminosity functions (LFs) for sources in the FLAMINGOS IC 348 region by using relatively wide (0.5 mag) bins and by restricting the sources to those in an area bounded by the  $10.33'$  radius. When we compared the  $J$ ,  $H$  and  $K$  band IC 348 LFs, we found that all of them display a double peaked structure: the first peak lying at  $J = H = K = 13 \sim 13.5$  and the second between  $J = 17.5$  and  $K = 16.5$ . Following our analysis of the cluster’s color-magnitude diagrams in Section

---

<sup>9</sup>From this source matching, we find that the NTC00 coordinates are systematically offset  $1/5$  south relative to the positional grid defined by 2MASS.

2.2.3, we interpret the brighter of these peaks to be sources in the IC 348 cluster and the fainter peak to be dominated by background field-stars and galaxies.

In Figure 8, we show the  $K$  band LFs of the IC 348, breaking the cluster into the “core” and the “halo” sub-regions and scaling them to stars per square degree. Further, we compare them to the un-reddened field-star KLF constructed from our off-cluster  $K$  band datasets. Confirming our preliminary study of the cluster’s structure from the radial profile, both sub-regions display a considerable excess of sources relative to the field-star KLF for  $m_K < 15$ . Both sub-region KLFs reach bright peaks although they occur in somewhat different locations with the core KLF, for example, peaking 1.5 magnitudes brighter than the halo. Below these bright peaks, both KLFs flatten or turnover before rising, parallel to the field-star KLF. While the faint KLF peak of the two sub-regions have nearly identical size and structure, they appear to be smaller and shifted to fainter magnitudes than the field-star KLF. Such differences could certainly be caused by the reddening and obscuration of background field-stars due to the molecular cloud. Thus, we used our detailed study of the cluster reddening properties (Section 2.4) to estimate the size of the field-star contribution to the observed KLFs.

### 3.2. Field-Star Correction to the Cluster KLF(s)

To statistically estimate the field-star contribution to the raw IC 348 KLF(s), we used a Monte Carlo integration to convolve this control KLF with the effects of a reddening probability distribution function that characterizes the the molecular cloud. We treated the cluster’s core and halo sub-regions separately, and we used the extinction probability distribution functions derived in Section 2.4 from the fainter, likely background stars de-reddened to the M dwarf locus. In Figure(s) 9ab we compare the raw KLFs to the reddened field-star KLFs appropriate to that sub-region, scaling the reddened field-star KLF *only* by the ratio of the off-cluster area to the physical area of the cluster or sub-region.

The reddened field-star KLFs very closely match the raw KLFs for  $m_K > 15$  in both sub-regions, although they exceed the cluster KLFs at the faintest magnitudes because they were not filtered to match our detection limits. We subtracted these reddened field-star KLFs from the raw cluster KLFs, and display the resulting differential KLFs in Figures 9cd, constructing error bars that are the  $1\sigma$  counting statistics of the sum of the cluster and reddened field star KLFs. The structure of the differential KLFs is significant for the bins brighter than  $m_K = 16.75$ , below which the field-star correction clearly over-estimates the observations. This magnitude limit corresponds to a  $10 M_{Jup}$  brown dwarf at the 2 Myr mean age we assumed for IC 348. Above this limit two sub-regions have a nearly identical number of members, with the core containing  $153 \pm 16$  sources with  $m_K \leq 15.25$  ( $172 \pm 24$ ;  $m_K \leq 16.75$ ) and the halo containing  $150 \pm 23$  sources with  $m_K \leq 15.25$  ( $176 \pm 40$ ;  $m_K \leq 16.75$ ). While the sub-region KLFs are well populated for  $m_K < 15$ , at fainter magnitudes the substantial field-star corrections yield very large uncertainties in the KLF structure.

In Figure 10 we directly compare the sub-region differential KLFs and sum them to construct the overall cluster KLF. Again, the differences in the structure of the two sub-region KLFs are obvious to the eye, with the peak of the halo KLF skewing significantly to fainter magnitudes, before strongly turning over.

While the peaks of the sub-region KLFs are clearly distinct, the KLFs are similar to within their  $1\sigma$  error bars in most bins but separated by 2 to  $3\sigma$  in the  $m_K = 11$  and  $m_K = 13$  bins. A two sample chi-square test of the two histograms (range:  $m_K = 8 - 15$ ) yielded a probability of 0.04 that they are drawn from the same parent distribution, indicating that these sub-region KLFs are different at the  $2\sigma$  level.

When the two sub-region KLFs are summed together, the complete cluster KLF has a very broad peak between  $m_K = 11.5 - 13$  before decreasing very sharply to  $m_K = 15$ . For the combined cluster KLF Despite the large uncertainties at faint magnitudes the composite KLF has a statistically significant number of cluster members with  $m_K > 15$ . Further, we found that if we increased the size of the field-star correction by using a bluer extinction distribution function (one relevant for the cluster stars), the main cluster KLF characteristics were not substantially altered, although the size of the very faint population is almost halved.

#### 4. The Initial Mass Function of IC 348

To analyze the IC 348 differential  $K$  band luminosity function(s) constructed in Section 3 we used our model luminosity function algorithm first presented in Muench, Lada & Lada (2000) and expanded in Paper I. Our goal was to place constraints on the initial mass function of IC 348 by deriving that mass function or set of mass functions whose model luminosity functions best fit the cluster KLF. For the purpose of comparing our work to other studies, we individually analyzed the KLFs of the two cluster sub-regions as well as the composite cluster KLF. Since a young cluster’s luminosity function is the product of an age dependent mass-luminosity relation and the cluster’s IMF, we examined both the star forming history of IC 348 as derived by existing spectroscopic studies (Section 4.1) and the appropriate theoretical mass-luminosity relations (Section 4.2). We then fixed these quantities and derived the cluster IMF (Section 4.4).

##### 4.1. The Star Formation History of IC 348

To derive accurate mass function for a young, partially embedded cluster, our method requires a good estimate of the cluster’s mean age (Muench, Lada & Lada 2000). We examined published spectroscopic studies of IC 348, which provide individual age estimates for a reasonable large number of members. In Figure 11, we plot a histogram of the ages derived by Herbig (1998) using the de-reddened  $V/V - I$  color-magnitude diagram for candidate pre-main sequence members in an 112 square arc-minute region of IC 348. We merged the ages of stars with and without detectable  $H\alpha$  emission and derived an ensemble cluster mean age of  $\sim 2$  Myr. We approximated the age spread of IC 348 to be  $\sim 3$  Myr, corresponding to constant star formation from 0.5 to 3.5 Myr ago, and we note that this age spread is 2.5 times longer than that we approximated for the younger Trapezium Cluster. We show in Figure 11 that our assumed star forming history closely approximates the bulk of the Herbig SFH, but clips the “older” tail of this distribution.

We did not include this “older” tail in our SFH of IC 348 for the following reasons: 1) Observational uncertainties (for example, membership criteria or errors in photometric and spectral classification) in the derivation of de-reddened color-magnitude or theoretical HR diagrams lead to exaggerated star forming

histories, specifically resulting in artificially inflated cluster’s age spreads (Hartmann 2001; Kenyon & Hartmann 1990); 2) A number of the “oldest” IC 348 objects analyzed in the NTC00 NICMOS study were also found to be the reddest cluster objects, suggesting to us that they are background interlopers; 3) Our assumed age spread very closely approximates that SFH derived by Palla & Stahler (2000), who found that the star formation in IC 348 began approximately 3 Myr ago with negligible star formation at older ages, and finally; 4) Model luminosity functions are very insensitive to the assumed age spread (Muench, Lada & Lada 2000). Further, Palla & Stahler found no dependence of the SFH on location within IC 348. Thus, we used the same star formation history when modeling both the ensemble cluster and the cluster’s “core” and “halo” sub-region KLFs.

#### 4.2. The Cluster Distance and the Mass-Luminosity Relation

Herbig (1998) included an extensive discussion on the distance to IC 348 based upon literature sources existing at that time. Arguing that closer distances ( $\sim 260$  pc) were systematic under-estimates, he chose a distance for IC 348 (320 pc) based in part upon the fact that within the current uncertainties, one could not differentiate between the distance to IC 348 ( $316 \pm 22$  pc Strom et al. 1974) and to the Perseus OB2 association Borgman & Blaauw ( $322 \pm 30$  pc 1964). Recent studies of this regions using Hipparcos data do not appear to have resolved the distance uncertainty between the Perseus OB2 association and the IC 348 cluster. de Zeeuw et al. (1999) derived a distance of  $317 \pm 27$  pc for 17 members of the Perseus OB2 association spread over a projected  $37 \times 37$  pc area, while also statistically estimating the number of interlopers. A study by Belikov et al. (2002), including a larger subset of probable members, seems to confirm this distance to the OB association. On the other hand, when Scholz et al. (1999) performed a recent proper motion study of the IC 348 region, they derived a distance of  $\sim 261$  pc using a set of 9 Hipparcos sources. This latter distance estimate to IC 348 should probably be treated with some caution. Since more than half of these 9 sources with parallaxes were at projected distances of 2.5 - 8 pc from the cluster center, they fall well outside any cluster outer radius we have discussed here and may not be actual members, especially since no statistical estimate of the number of non-members was performed for the Scholz et al. study. Further, Ripepi et al. (2002) very recently reported the discovery of an F star within the IC 348 boundaries that displays rapid  $\delta$  Scuti-like variability that is interpreted as the pulsation of a PMS star while in its instability strip (Marconi & Palla 1998). The derived pulsation period strongly favors a distance of  $\sim 320$  to IC 348. Thus, it remains unclear if the distance to IC 348 can be separated from the distance to the OB association. For our modeling we adopted the distance of 320 pc ( $m-M = 7.5$ ) to IC 348 for consistency with the work of LL95 and Herbig (1998), but we examined how such a distance uncertainty could affect our results.

Such distance uncertainties may systematically affect the derivation of cluster properties such as mean age and possibly the IMF. Herbig, for example, showed that assigning IC 348 a closer distance yielded a systematically older cluster mean age since the cluster appears intrinsically fainter when compared to pre-main sequence evolutionary models. In Figure 12, we examine the net effect of this age-distance uncertainty on the theoretical mass-luminosity relations relevant for our luminosity function modeling. Shifting the distance from 320 to 260pc produces a shift in the mean age from 2 to  $\sim 3-4$  Myr (see also Haisch, Lada,

& Lada 2001). However, the change in the distance modulus ( $-0.42$  magnitudes) is roughly equivalent to the average luminosity evolution of stars ( $1.0 - 0.1 M_{\odot}$ ) between 2 and 3 Myr ( $dK \sim -0.35$ ). By comparing the mass- $K$  magnitude relation at 2 Myr and 320pc to that at 3 Myr and 260 pc, we find that above the hydrogen burning limit, our derived IMF will have little systematic dependence upon the cited age-distance uncertainty for IC 348 and should be a faithful representation of the true cluster IMF. On the other hand, the slope of the substellar mass- $K$  magnitude relation is systematically affected, in part due to a larger mass range undergoing deuterium burning. Thus, our derived substellar IMF will be less reliable than the stellar IMF until this age-distance uncertainty is resolved.

Lastly, in Figure 12 we also compare the theoretical mass-luminosity relations taken from two sets of evolutionary calculations. As we found in Paper I, different theoretical mass- $K$  magnitude relations are very consistent between current sets of PMS tracks, meaning that the derived IMF will be mostly independent of which set of modern PMS models we use. To provide consistency between our studies of various young clusters, we derived the cluster IMF using our standard set of PMS tracks, which are primarily based on the D’Antona & Mazzitelli (1997) tracks and whose construction and conversion to observable quantities were described in Muench, Lada & Lada (2000).

### 4.3. Other Modeling Parameters: Reddening and Binaries

Three additional characteristics of young stars that we can include into our model luminosity function algorithm are the reddening of the cluster members by the parental molecular cloud, excess infrared flux due to optically thick disks around the cluster members, and the frequency of un-resolved companions. First, to account for the reddening of the cluster by the Perseus Molecular Cloud, we used the extinction distribution functions derived in section 2.4 for the bright cluster stars de-reddened to the cTTS locus.

Second, in Section 2.2.3 we confirmed the LL95 finding of  $\sim 60$  infrared excess sources distributed across the IC 348 cluster region. Correcting for field stars and dividing the excess sources by sub-region, we found infrared excess fractions of  $14 \pm 11\%$  (22/153) for the core sub-region,  $24 \pm 17\%$  (36/150) for the cluster halo and  $19 \pm 10\%$  (58/303) for the composite cluster. If we restrict these estimates to those 42 sources which have NIR excess greater than their  $1\sigma$  photometric errors, these percentages drop to 9%, 14% and 11%, respectively. Because these excess fractions are very small, we chose to no account for NIR excess in our KLF models of IC 348. It is possible, however, that a more substantial fraction of sources could have small  $K$  band excesses ( $dK_{irx} \sim 0.1$ ) that are not apparent in the color-color diagram especially since Haisch, Lada, & Lada (2001) found that 65% of the IC 348 members have inner circumstellar disks as traced at  $3\mu\text{m}$ . We argue such small excesses will not substantially affect the cluster KLF and hence the derived cluster IMF since this flux excess is much smaller than the bins used to create the cluster luminosity function.

Finally, we choose not to include un-resolved binaries into our modeling of IC 348, paralleling our analysis of the Trapezium Cluster in Paper I. Thus, the IC 348 IMF we derive is the “primary” or “single” star IMF. Duchêne, Bouvier & Simon (1999) found that the binary fraction in IC 348 is very similar to

that found in other young clusters and to the field. Further, the consistency of the binary frequency in stellar clusters over a large range of cluster age (Patience et al. 2002), including young clusters like IC 348, suggests that the single star IMFs of star clusters can be readily derived and compared without correction for binaries.

A related issue in our studies of different cluster IMFs is whether or not a significant fraction of *resolved* wide binaries have been included into the cluster KLFs. For example, the physical resolution of our Trapezium study was  $\sim 240$  au, while in IC 348 it is  $\sim 480$  au. Since the binary fraction at these large separations is quite small ( $f < 0.1$ ), the few resolved binary systems that will be included into these cluster KLFs should not significantly modify the single star IMFs we derive.

#### 4.4. Modeling the IC 348 Differential KLF(s)

Using these cluster parameters, we produced a suite of model luminosity functions by varying the underlying initial mass functions. Our goal is to find the simplest underlying IMF or range of IMFs whose model luminosity functions best fit the observed cluster KLF(s). Our standard IMF parameterization consists of power-law segments,  $\Gamma_i$ , connected at break masses,  $m_j$ , and we use the fewest segments necessary to fit the model KLF, which for IC 348 resulted in 2 and 3 segment IMFs. We independently calculated and fit model luminosity functions for both the composite cluster KLF and the cluster’s “core” and “halo” sub-region KLFs, varying the extinction distribution function appropriately for each region. Our fitting technique calculates the  $\chi^2$  statistic and probability between the model KLFs and observed KLF over a range of magnitude bins and from these statistical measures, the parameters (mean, standard deviation) of the underlying IMF are derived. We summarize these fits and the resulting IMFs for the complete cluster in Section 4.4.1, and for the two sub-regions in Section 4.4.2

##### 4.4.1. The Composite IC 348 KLF

We examine the best fit model KLFs to the complete cluster KLF in the left hand panel of Figure 13. The composite cluster KLF displays a very broad main peak followed by a sharp turnover at fainter magnitudes. This structure required the use of model KLFs based upon a 3 power-law underlying IMF, and we tabulate the derived IMF parameters in Table 3. By varying the range of KLF bins fit by our  $\chi^2$  routine, we find that with these 3 segment underlying IMFs we were able to fit the composite cluster KLF down to  $m_K = 15$ , constraining the cluster IMF from  $2.5M_\odot$  down to  $\sim 0.035M_{Jup}$  (for  $\langle A_V \rangle = 4$ ). Non-power-law structure in the cluster KLF for  $m_K > 15$  prevented decent fits to these bins (see Section 5.1.2).

Over this  $m_K - M$  fit range, our KLF fits yielded an IC 348 IMF having a broad peak down to the hydrogen burning limit before rolling over and decreasing sharply into the substellar regime. The high mass  $\Gamma_1$  slope was moderately constrained with an index of  $\sim -1.5 \pm 0.3$  (Salpeter =  $-1.35$ ) before flattening at  $m_1 = 0.80M_\odot$ . The  $\Gamma_2$  slope and the  $m_2$  mass break are both strongly constrained by the broad KLF peak and the sharp KLF turnover at  $m_K = 13$ , with a very slowly rising  $\Gamma_2 \sim -0.2 \pm 0.15$  across much of

the IMF before peaking at the hydrogen burning limit. Because of the rapid change in KLF slope between  $m_K = 12-15$ , there is a moderately large uncertainty in  $\Gamma_3$  IMF parameter with a sub-stellar IMF slope that is very steeply falling with an index of  $\sim +2.0 \pm 0.4$ .

#### 4.4.2. The IC 348 Core and Halo Sub-Region KLFs

In the left hand panels of Figure 14 we display the sub-region differential KLFs compared to the best fit model KLFs derived from our  $\chi^2$  fitting technique. The underlying power-law IMFs are displayed in the right hand panels of this figure, and we list our derived IMF parameters in Table 3 as a function of fit range.

Unlike the more complex structure of the composite cluster KLF, we found that model KLFs constructed using 2 power-law IMFs provided satisfactory fits to both sub-region KLFs, although we were able to obtain slightly better fits to the “halo” KLF using a 3 segment IMF. For both sub-regions, the  $m_1$  mass break was very strongly constrained by the location of the bright KLF peaks in the 2 power-law IMF fits. The  $\Gamma_1$  IMF slope rises steeply with decreasing mass in the “core” sub-region, but is much shallower in the “halo” region. In our 3 power-law fits to the “halo” sub-region, we found a modest  $\chi^2$  minima that indicated there is an inflection in this high mass slope near  $0.80M_\odot$ , yielding a  $\Gamma_1$  similar to that found in the 2 segment “core” IMF and to the composite cluster IMF (see Table 3 for comparison of 2 and 3 segment IMFs for IC 348). As evident in their KLFs, the two sub-regions have distinctly different IMF peaks regardless of the complexity of the underlying IMF, with the core  $m_1$  mass break occurring at  $0.56 \pm 0.18M_\odot$  and the peak of the halo IMF strongly constrained to lie at  $0.10 \pm 0.02M_\odot$ . Below their peaks, both sub-region IMFs steadily fall with decreasing mass down to the  $m_K - M$  fit limit, which for both sub-regions corresponded to at least the  $m_K = 15$  bin and a minimum fit mass of  $0.035M_\odot$ . The  $\Gamma_2$  slope was more tightly constrained for the two power-law “core” IMF than for the halo, and we found that a single power-law IMF with slope of  $\Gamma \sim 0.4$  could fit the core KLF from the IMF peak ( $\sim 0.5M_\odot$ ) all the way down to the  $m_K = 16.5$  bin, which has a lower  $m_K - M$  limit from the DM97 tracks of  $0.017M_{Jup}$ . Similar to the composite cluster IMF, the rapid change in halo KLF slope between  $m_K = 12-15$  yielded considerable uncertainty in the corresponding IMF parameter below the halo IMF peak, but it was constrained to be steeply falling, with a  $\Gamma_{bds,halo} \sim 2.0$ . Despite any limitations to our fitting procedure, we found that while the resulting substellar IMF slopes are different in the two sub-regions ( $\Gamma_{bds,halo} \sim 2.0$  versus  $\Gamma_{bds,core} \sim 0.4$ ), they correspond to similar proportions of brown dwarfs between the two regions, as we will discuss further in Section 5.3.

## 5. Discussion

### 5.1. The KLFs and IMFs of IC 348 and the Trapezium

#### 5.1.1. The Stellar Regime

We examined the structure of the IC 348 KLF and derived IMF by comparing these characteristics to those we derived for the Trapezium cluster in Paper I. By comparing the Paper I Trapezium IMF (also reproduced in Table 3) to the derived IC 348 IMF we find that these two very young clusters have nearly identical IMFs throughout the stellar regime. As illustrated in Figure 13, both clusters have IMFs that rise in number with decreasing mass into the sub-solar regime, with Salpeter-like power-law slopes ( $\Gamma_{1, Trap} = -1.21$  and  $\Gamma_{1, IC348} = -1.53$ ). Their IMFs both flatten around  $0.7M_{\odot}$ , having slopes of  $\Gamma_2 \sim -0.2$  and form very broad shallow peaks at sub-solar masses. The “peak” or mode of their IMFs varies between  $0.15$  and  $0.08M_{\odot}$  with a skewing of the mode of the IC 348 IMF to slightly lower masses than the Trapezium IMF, although this may be due to the Trapezium being only core of the larger Orion Nebula Cluster (see Section 5.3).

The strong similarities between these clusters’ stellar IMFs exist despite the significant apparent differences between their cluster KLFs. In Figure 15a, we compare the Trapezium and IC 348 KLFs, shifting them by their respective distance moduli to absolute magnitudes and scaling the size of the Trapezium population to match that of IC 348. The IC 348 KLF is clearly broader and shifted to fainter magnitudes relative to the Trapezium KLF with their primary KLF peaks differing by almost 2 magnitudes. These differences, however, are precisely those predicted by the evolution of the luminosity function with age (Lada & Lada 1995; Muench, Lada & Lada 2000). Indeed if we evolve a model KLF of the younger Trapezium to the age of IC 348 and compare it to the IC 348 KLF in Figure 15b, we find it agrees with the observed IC 348 KLF extremely well down to  $m_K = 12.5$ , near the unreddened hydrogen burning limit for IC 348 ( $\tau = 2$  Myr,  $m_{K, HBL} \sim 12.7$ )<sup>10</sup>. Fainter than this magnitude the evolved Trapezium KLF moderately under-estimates the IC 348 KLF between  $m_K = 13 - 13.5$ , indicative of the slight skewing of the mode of the derived IC 348 IMF to lower masses. Below  $m_K = 13$ , both the observed IC 348 KLF and the evolved Trapezium KLF steeply fall in number, marking the transition to the substellar regime that we explore in the next section.

#### 5.1.2. The Sub-Stellar Regime

Reviewing Figure(s) 13b and 15, one immediate similarity between the substellar KLFs and IMFs of IC 348 and the Trapezium is their mutual steep decline towards fainter magnitudes and lower masses. Although the IC 348 IMF mode skews to lower masses than the Trapezium, it turns over and decreases in a much steeper manner than the Trapezium, i.e.,  $\Gamma_{BDs, IC348} = 2.0$  while  $\Gamma_{BDs, Trap} \sim 0.7$ . This is also

---

<sup>10</sup>This quantity is fairly independent of current PMS tracks, see Figure 12. From various models we find for IC 348 that  $m_{K, HBL}(D’Antona \& Mazzitelli 1994) = 12.74$ ,  $m_{K, HBL}(DM97) = 12.67$ ,  $m_{K, HBL}(\text{Burrows et al. 1997}) = 12.55$ , and  $m_{K, HBL}(\text{Baraffe et al. 1998}) = 12.83$ . For a mean age of 3 Myr at a distance of 260 pc,  $\langle m_{K, HBL} \rangle = 12.68$ .

illustrated by the way that the evolved Trapezium KLF seems to consistently over-estimate the number faint objects in IC 348, although they agree within the large statistical uncertainties.

A second similarity between the substellar KLFs of IC 348 and the Trapezium, is the formation of a modest secondary KLF peak. After correction for background stars we estimate that in IC 348 this secondary KLF peak contains  $42 \pm 29$  sources between  $m_K = 15 - 17$ . Further, the secondary KLF peak for IC 348 occurs precisely in the magnitude range predicted by the evolved Trapezium KLF (see Figure 13b), suggesting they are related features and correspond to sources in the mass range from  $10 - 20M_{Jup}$ . As was the case for our Trapezium modeling, such KLF structure rejected our fitting of these magnitude bins using models based upon 3 segment power-law IMFs. This is because we are trying to fit this non-power law KLF structure (a dip or gap followed by a secondary peak) with model KLFs that are essentially a power-law throughout the brown dwarf regime because the theoretical mass-luminosity relations that we have used are smooth and do not contain any significant evolutionary features in this mass range. Considering the statistical uncertainties due to the background correction we did not attempt to explicitly fit additional IMF segments to the IC 348 peak although the size of the predicted peak using the Trapezium IMF closely approximates this feature. We discuss the origin of this secondary KLF peak further in Section 5.2.

One meaningful constraint regardless of detailed IMF structure is the *fraction* of cluster members that are substellar. For example, in the Trapezium we found that  $22^{+4}_{-2}\%$  of the clusters members fell between 80 and  $17M_{Jup}$ , having the interesting implication that only  $\sim 1$  in 4 of the cluster members were brown dwarfs! Estimating this fraction for IC 348 was more difficult because the background correction makes directly counting all the substellar sources difficult. Rather than directly counting sources, we first integrated the derived IMF to calculate the fraction of substellar sources down to the mass limit of our fit. We found that brown dwarfs between 80 and  $25 M_{Jup}$  (the lower mass limit for  $A_V = 0$  and corresponding to our model fits to  $m_K = 15$  and the beginning of the secondary KLF peak) constitute only 14% of the members with 2% uncertainty due to the variation in our fits, and 9% uncertainty due to the counting statistics which are dominated by the size of the background correction. For comparison, integrating the Trapezium IMF over the same mass range yields a brown dwarf fraction of 20%.

When we count the number of sources contained in the secondary peak of the IC 348 KLF and not included into the KLF fits, we were able to extend the range of substellar masses down to  $10M_{Jup}$ , however we also found that the precision of our estimate is significantly worsened by the large field star contamination. Since this secondary KLF peak contains between 26 and 42 sources depending upon the size of the correction for field stars, the total substellar fraction increased to 20–25% for IC 348, although the corresponding error bar also increased to  $\pm 14\%$ . Thus, despite the uncertainties due to the field star correction these fractions indicate that IC 348 has a very similar brown dwarf fraction to that found for the Trapezium and further, that brown dwarfs are not nearly as populous as stars in either cluster.

## 5.2. The Secondary Sub-Stellar Peak in the Cluster KLFs

As we derived in Paper I, the secondary peak in the Trapezium KLF can be attributed to a corresponding IMF peak near the deuterium burning limit. Our finding of an IC 348 KLF feature having a similar size and corresponding to the same mass range,  $10-20M_{Jup}$ , lends some support to this conclusion. One interesting implication of such structure in the cluster’s substellar IMF would be the existence of a separate formation mechanism for very low mass brown dwarfs, as we postulated in Paper I. However, since the LF is the product of the IMF and the slope of the mass-luminosity relation, it may also be the case that a subtle feature or inflection exists in the empirical mass-luminosity relation that has not been resolved by even the most recent theoretical models of brown dwarfs (e.g., Chabrier et al. 2000; Baraffe et al. 2002). Such an unaccounted for M-L feature could also produce features in the LF independent of the structure of the underlying IMF, as previously found, for example, in the Kroupa, Tout & Gilmore (1990, 1993) studies of the  $H^-$  and  $H_2$  opacity features in the optical  $M-M_V$  relation for field stars.

There is very recent observational evidence that seems to point toward an unaccounted for M-L feature for brown dwarfs. Dobbie et al. (2002) discuss a feature in the color-magnitude diagram for the Pleiades Cluster, corresponding to an apparent gap in both color and luminosity space for substellar objects. Dobbie et al. (2002) draw an analogy between this feature and the  $H^-$  opacity related Wielen gap (Kroupa, Tout & Gilmore 1990), attempt to correct the theoretical mass-luminosity relation for the effect of such a gap, and conclude that the lack of this feature in the theoretical tracks (which they suggest is related to the formation of dust in the brown dwarf atmospheres) is likely the cause of the IMF structure we derived for the Trapezium in Paper I and that was also derived for the IMF of the  $\sigma$ -Orionis cluster by Béjar et al. (2001). We point out that what we observe in the Trapezium and IC 348 appear to be secondary peaks in the cluster KLFs. Drawing an analogy to studies of the  $H_2$  opacity feature in the field star mass-luminosity relation (Kroupa, Tout & Gilmore 1993; Kroupa & Tout 1997) or to the effects of deuterium burning on theoretical model KLFs (Zinnecker et al. 1993; Muench, Lada & Lada 2000) such a peak could be caused by a piling up of stars with a range of mass in a narrow range of luminosity. If we were to repeat the Dobbie et al. (2002) correction to the theoretical M-L relation but assume a more steeply falling slope for the substellar IMF of the Pleiades, such an inflection or piling up would be the result.

Regardless, it is uncertain which effect (IMF, M-L relation) will in fact dominate the nature of the secondary KLF peaks we have observed. Clearly, improvements are needed in the theoretical tracks, which, in combination with future observations, should be able to disentangle these two effects for the substellar IMFs of young clusters. However, which mechanism is producing this KLF peak appears to operate only at the very lowest masses in the very young ( $\tau < 10$  Myr) clusters we are studying. Thus, it seems unlikely that it will modify the derived IMF at the hydrogen burning limit and future updates probably will not adjust (inflate or decrease) the percentage of sources that are brown dwarfs in these clusters.

### 5.3. Radial Variation of the IC 348 IMF

Our division of the cluster into two sub-regions based on the cluster’s radial profile (see Section 2.3.1) allowed us to make important comparisons to past studies of the IC 348 IMF, which have primarily focused on the cluster’s core. For example, when we compare in Figure 16 the IMF we derived for around 150 sources in the IC 348 “core” to those MFs derived by NTC00 and Luhman et al. (2000) each containing 90-100 sources, we find they agree remarkably well, all having an IMF that peaks or has a mode between 0.3 and 0.5  $M_{\odot}$  and turns over into the substellar regime. Those differences that do exist between our “core” IMF and these studies are likely due to the 50% difference in sample sizes, which may produce statistical fluctuations, or source saturation in the NICMOS study, which causes it to exclude higher mass stars.

Such a strong similarity is not found, however, when we compare the IMF of the cluster’s core (derived in this or past studies) to that we derived for the cluster halo. Paralleling the apparent physical differences in the KLFs of the IC 348 sub-regions (see Figures 8 and 10), we find that the IMF of the halo skews to lower masses relative to the IMF of the cluster’s core. This variation of the IMF is a real representation of the differences in the two sub-regions and is not the product of a variation in some other physical quantity. Reddening due to the molecular cloud and specific to each sub-region is included into these fits, although no meaningful differences exist between the relevant EPDFs of the two regions (see Section 2.4.2). Although we did not include the effects of infrared excess, any such effect would actually *increase* the IMF differences, since the larger excess fraction of the halo and would require the halo IMF peak to shift to lower masses. Further, the larger excess fraction in the halo might imply that the halo is younger than the core. However, accounting for such an age difference would again shift the IMF peaks in *opposite* directions from one another and amplify the IMF variations we derive. Lastly, although it would seem to contradict the distribution of infrared excess and  $H\alpha$  sources and was not corroborated by the study of Palla & Stahler (2000), Herbig (1998) reported a slight age gradient in IC 348, finding an increasing mean age at larger radii. Such a gradient does act in the correct direction to account for some of the KLF differences, however, even if this age gradient is real, it is considerably too small ( $\tau \sim 1.45$  Myr at  $R = 4'$  to 2.8 Myr at  $R = 10'$ ) to bring the IMFs of the sub-regions into agreement. To align the sub-region IMF peaks given the observed KLFs would require two distinct populations where the halo is 5-10 Myr older than the core. This is an difficult hypothesis to accept considering the populations are of equal size, and while such a model might align the peak of the IMFs by shifting the halo to higher masses, it would further imply that the IMF of the halo is truncated below 0.3  $M_{\odot}$ . As was originally found in the model fits of LL95, we conclude that such a two age population model cannot explain the IC 348 KLFs. Indeed, the one physical phenomena that we cannot test here, the fact that the “core” sub-region contains “halo” members due to the two dimensional projection of the cluster, implies a priori that the spatial IMF variation are *larger* than we derive since the “halo” IMF contaminates the cluster “core”(but not the reverse).

Since differences between the core and halo sub-region KLFs can only be related to their underlying IMFs and these IMF differences (as illustrated in Figure 16) appear statistically significant at the  $2\sigma$  level, we conclude that a physical variation in the IC 348 IMF appears to exist on spatial scales of the order of 1 parsec. Further, these radial IMF differences primarily occur in a limited range of sub-solar masses between 0.5 and 0.08  $M_{\odot}$  in IC 348. This radial IMF variation is unlike typical scenarios for mass segregation in very

young clusters in which only the higher mass stars ( $M > 1M_{\odot}$ ) are thought to be preferentially affected. With these cluster(s) being only a few crossing times old, there is thought to be only enough time for the massive stars to sink to the cluster core (Kroupa, Aarseth & Hurley 2000); otherwise, these more massive stars are thought to be preferentially born in the cluster center through a process of competitive accretion (Bonnell, Bate, Clarke, & Pringle 2001).

Radial variations of a cluster’s sub-solar IMF have also been reported for the Orion Nebula Cluster(ONC), of which the Trapezium is the core. While this cluster displays additional evidence for the segregation of high mass stars to the cluster core (Hillenbrand & Hartmann 1998), the low mass ONC IMF varies between the central core and outer cluster halo. This has been shown by Hillenbrand (1997) and Hillenbrand & Carpenter (2000) who found that while the IMF of the central  $r < 0.35$ pc Trapezium core peaks around  $0.2M_{\odot}$ , the addition of the cluster’s halo ( $r_{tidal} = 2.5$ pc) produces a composite ONC IMF that continues to rise down to  $0.1M_{\odot}$ , the completeness limit of the Hillenbrand spectroscopic survey of the entire ONC cluster. Thus, this skewing of the stellar IMF with radius proceeds in the same direction in the ONC as we find in IC 348, although IC 348 may in fact be a better location for studying such mass segregation. This is because the ONC is projected along the same line of sight as the Orion Ic OB association, which may contaminate the derived cluster IMF at large radii. What is clear in both clusters is that meaningful comparisons of their IMFs can only be performed after composite IMFs have been derived over large physical areas of the clusters; smaller areas are subject to mass segregation effects even at very young ages. Further, such effects must be taken into account when placing them into discussion of a “universal” IMF (see also Kroupa 2002).

Lastly, it is important to examine how the substellar sources are radially distributed. Since dynamical effects that could produce the radial IMF variation may operate on the lowest mass sources by skewing them to larger radii, brown dwarfs may correlate with the distribution of low mass,  $0.1 - 0.3M_{\odot}$  sources and be systematically located further from the cluster center. While the slope of the substellar IMF varies significantly between the IC 348 core and halo, the percentage of sources that are substellar does not. We found that sources in the mass range from  $80 - 25M_{Jup}$  constitute roughly 14% of the sources in the cluster core and a similar 16% in the cluster halo (poissonian error for both fractions is  $\sim 10\%$ ). This finding suggests that the mechanism that is breaking the universality of the IMF on small spatial scales, whether it is primordial IMF variations or dynamical mass segregation, does not appear to be significantly acting upon the substellar population. Wide-field infrared imaging of other young clusters, such as, for example, a survey of the substellar population in the ONC halo, will be necessary to determine if similar, uniform spatial distributions of brown dwarfs exist in other clusters that are still embedded in their parental molecular clouds.

## 6. Conclusions

Using wide-field near-infrared images provided by the FLAMINGOS camera on the Kitt Peak 2.1m telescope, we performed a detailed census of the young 2 Myr IC 348 cluster located on the northeastern end

of the Perseus Molecular Cloud. Using the multi-color infrared photometry provided by our observations, we explored this cluster’s structure, reddening, and relationship to the parental molecular cloud, and then used these results to construct and to analyze the IC 348 KLF and to correct it for field star contamination. Using our model luminosity function algorithm described in Muench, Lada & Lada (2000) and Muench et al. (2002), we derived the cluster’s initial mass function, providing detailed fits and error estimates. From our analysis of the cluster’s structure and luminosity function and by comparison to our earlier study of the Trapezium cluster, we draw the following conclusions about the KLF and IMF of IC 348:

1. We derive an IMF for the composite IC 348 cluster spanning the mass range from  $2.5$  to  $0.035M_{\odot}$ . Further, we find that the IC 348 IMF we derive is nearly identical to the Trapezium IMF we derived in Paper I: The two clusters’ IMFs rise with decreasing mass, having a Salpeter-like slopes before flattening below  $0.7M_{\odot}$ . Within the current uncertainties in PMS evolutionary models, we find that the mode of these star cluster IMFs appear to fall at a mass of  $\sim 0.1-0.2M_{\odot}$ .
2. Further, we find that the relative size of the substellar population is very similar in both clusters within the uncertainties of our method, revealing that brown dwarfs constitute between 15–25% of the members of either cluster and do not dominate the cluster’s stellar populations.
3. IC 348 forms a modest but significant secondary KLF peak, corresponding to sources in the same mass range that we found responsible for a similar secondary KLF peak in the Trapezium. The similar KLF features in the Trapezium and IC 348 may signify either the presence of a secondary peak in the substellar IMF between  $10-20M_{Jup}$  as we derived in Paper I, or be the result of a previously unknown feature in the brown dwarf mass-luminosity relation (e.g., Dobbie et al. 2002).
4. Radial variations are found in the KLF and IMF of IC 348 on the parsec scale, with a skewing of the KLF to fainter sources and the IMF to lower mass stars in the cluster’s halo, a portion of the cluster whose IMF was previously undetermined. This radial variation in the sub-solar IMF is similar to but more pronounced than what was found previously for the sub-solar mass stars in the Orion Nebula Cluster. It is unclear what process is breaking the universality of the cluster’s IMF on small spatial scales, but it appears different from dynamical mass segregation which primarily acts upon higher mass stars at these young ages. Further, while the slope of the substellar IMF varies as a function of radius in IC 348, the spatial distribution of brown dwarfs in this cluster is different from the stars and is uniformly distributed between the cluster’s core and halo.

Finally, we draw the general conclusion that the existence of radial variations of the IMF on parsec scales even at very young ages (1 Myr) may mean that wide-field imaging surveys are a pre-requisite to making meaningful IMF comparisons between different embedded clusters, a fact that has clearly been true in older open clusters for some time.

We would like to thank Simon Hodgkin for a discussion on the existence of a previously unknown feature in the substellar mass-luminosity relation. EAL and AAM acknowledge support from a Research

Corporation Innovation Award and Presidential Early Career Award for Scientists and Engineers (NSF AST 9733367) to the University of Florida. The FLAMINGOS camera was designed and constructed at the University of Florida under a grant from the National Science Foundation (NSF AST 9731180). The data for this paper were collected under the NOAO Survey program, “Toward a Complete Near-Infrared Spectroscopic and Imaging Survey of Giant Molecular Clouds” (E. Lada, P.I.). This publication makes use of data products from the Two Micron All Sky Survey, which is a joint project of the University of Massachusetts and the Infrared Processing and Analysis Center/California Institute of Technology, funded by the National Aeronautics and Space Administration and the National Science Foundation.

## REFERENCES

- Allard, F., Hauschildt, P. H., Alexander, D. R., Tamanai, A., & Schweitzer, A. 2001, *ApJ*, 556, 357
- Alves, J., Lada, C.J., Lada, E.A., Kenyon, S.J., & Phelps, R. 1998, *ApJ*, 506, 292
- Baraffe, I., Chabrier, G., Allard, F., & Hauschildt, P. H. 1998, *A&A*, 337, 403
- Baraffe, I., Chabrier, G., Allard, F., & Hauschildt, P. H. 2002, *A&A*, 382, 563
- Béjar, V. J. S., Martín, E. L., Zapatero Osorio, M. R., Rebolo, R., Barrado y Navascués, D., Bailer-Jones, C. A. L., Mundt, R., Baraffe, I., Chabrier, C., & Allard, F. 2001, *ApJ*, 556, 830
- Belikov, A. N., Kharchenko, N. V., Piskunov, A. E., Schilbach, E., & Scholz, R.-D. 2002, *A&A*, 387, 117
- Bertin E., & Arnouts, S. 1996, *A&AS*, 117, 393
- Bessell, M. S., & Brett, J. M. 1988, *PASP*, 100, 1134
- Bonnell, I. A., Bate, M. R., Clarke, C. J., & Pringle, J. E. 2001, *MNRAS*, 323, 785
- Borgman, J., & Blaauw, A. 1996, *Bull. Astron. Inst. Netherlands*, 17, 358
- Boulard, M.-H., Caux, E., Monin, J.-L., Nadeau, D., & Rowlands, N. 1995, *A&A*, 300, 276
- Burrows, A., Marley, M., Hubbard, W.B., Lunine, J.I., Guillot, T., Saumon, D., Freedman, R., Sudarsky, D., & Sharp, C. 1997, *ApJ*, 491, 856 (B97)
- Carpenter, J. M. 2000, *AJ*, 120, 3139
- Carpenter, J. M. 2001, *AJ*, 121, 2851
- Carpenter, J.M., Hillenbrand, L.A., & Strutskie, M.F. 2001, *AJ*, 121, 3160
- Chabrier, G., Baraffe, I., Allard, F., & Hauschildt, P. H. 2000, *ApJ*, 542, 464
- Cohen, J. G., Frogel, J. A., Persson, S. E., & Elias, J. H. 1981, *ApJ*, 249, 481
- D'Antona, F., & Mazzitelli, I. 1994, *ApJS*, 41, 467
- D'Antona, F. & Mazzitelli, I. 1997, *Cool Stars in Clusters and Associations*, ed G. Micela and R. Pallavicini, (Mem. S.A.It.), 68, 807
- de Zeeuw, P. T., Hoogerwerf, R., de Bruijne, J. H. J., Brown, A. G. A., & Blaauw, A. 1999, *AJ*, 117, 354
- Dobbie, P.D., Pinfield, D.J., Jameson, R.F., & Hodgkin, S.T. 2002, *MNRAS*, in press
- Duchêne, G., Bouvier, J., & Simon, T. 1999, *A&A*, 343, 831
- Elston, R. 1998, *Proc. SPIE*, 3354, 404

- Fruchter, A. S. & Hook, R. N. 2002, PASP, 114, 144
- Haisch, K. E., Lada, E. A., & Lada, C. J. 2001, AJ, 121, 2065.
- Hartmann, L. 2001, AJ, 121, 1030
- Herbig, G. H. 1998, ApJ, 497, 736
- Herbst, W., Maley, J. A., & Williams, E. C. 2000, AJ,
- Hillenbrand, L. A. 1997, AJ, 113, 1733
- Hillenbrand, L. A. & Hartmann, L. W. 1998, ApJ, 492, 540
- Hillenbrand, L. A. & Carpenter, J. M. 2000, ApJ, 540, 236
- Kenyon, S. J. & Hartmann, L. W. 1990, ApJ, 349, 197
- Kirkpatrick, J. D., Reid, I. N., Liebert, J., Gizis, J. E., Burgasser, A. J., Monet, D. G., Dahn, C. C., Nelson, B., & Williams, R. J. 2000, ApJ, 120, 447
- Kroupa, P., Tout, C. A., & Gilmore, G. 1990, MNRAS, 244, 76
- Kroupa, P., Tout, C. A., & Gilmore, G. 1993, MNRAS, 262, 545
- Kroupa, P. & Tout, C. A. 1997, MNRAS, 287, 402
- Kroupa, P., Aarseth, S., & Hurley, J. 2000, MNRAS,
- Kroupa, P. 2002, Science, 295, 82
- Lada, C. J., Lada, E. A., Clemens, D. P., & Bally, J. 1994, ApJ, 429, 694
- Lada, E. A., Evans, N. J., Depoy, D. L., & Gatley, I. 1991, ApJ, 371, 171
- Lada, E. A. & Lada, C. J. 1995, AJ, 109, 1682.
- Luhman, K. L., Rieke, G. H., Lada, C. J., & Lada, E. A. 1998, ApJ, 508, 347
- Luhman, K. L. 1999, ApJ, 525, 466
- Luhman, K.L., Reike, G.H., Young, E.T., Cotera, A.S., Chen, H., Rieke, M.J., Schneider, G., & Thompson, R.I. 2000, AJ, 540, 1016
- Marconi, M. & Palla, F. 1998, ApJ, 507, L141
- McCaughrean, M. J., Rayner, J. T., & Zinnecker, H. 1994, ApJ, 436, L189
- Meyer, M. R., Calvet, N., & Hillenbrand, L. A. 1997, AJ, 114, 233

- Muench, A. A., Lada, E. A., & Lada, C. J. 2000, *ApJ*, 533, 358 (MLL00)
- Muench, A. A., Lada, E. A., Lada, C. J., & Alves, J. 2002, *ApJ*, 573, 366 (MLLA02)
- Najita, J., Tiede, G., & Carr, J. 2000, *ApJ*, 541, 977 (NTC00)
- Palla, F., & Stahler, S. W. 2000, *ApJ*, 540, 255 (PS00)
- Patience, J., Ghez, A. M., Reid, I. N. & Matthews, K. 2002, *AJ*, 123, 1570
- Persson, S. E., Murphy, D. C., Krzeminiski, W., Roth, M., & Rieke, M. J. 1998, *AJ*, 116, 2475.
- Preiblich, T., Zinnecker, H., & Herbig, G. H. 1996, *A&A*, 310, 456
- Ripepi, V., Palla, F., Marconi, M., Bernaber, S., Arellano Ferro, A., Terranegra, L., & Alcalá, J.M. 2002, *A&A*, in press
- Salpeter, E. E. 1955, *ApJ*, 121, 161
- Scholz, R.-D., Brunzendorf, J., Ivanov, G., Kharchenko, N., Lasker, B., Meusinger, H., Preibisch, T., Schilbach, E. & Zinnecker, H. 1999, *A&AS*, 137, 305
- Strom, S. E., Strom, K. M., & Carrasco, L. 1974, *PASP*, 86, 798
- Tsuji, T., Ohnaka, K., Anoki, W., & Nakajima, T. 1996, *A&A*, 308, L29
- Zinnecker, H., McCaughrean, M. J., & Wilking, B. A. 1993, in *Protostars and Planets III*, ed. E. H. Levy & J. I. Lunine (Tucson: The University of Arizona Press), 429–495

Table 1. Summary of FLAMINGOS Observations of IC 348

Date	Julian Date	Target	Filter	Exp. (sec)	Dithers	Total Exp. (sec)	Airmass	Seeing ( $''$ )	$5\sigma$ (mag)	Flat-Field type
14 Dec 2001	2452257.82961	IC 348	<i>K</i>	20	49	980	1.139	1.60	16.81	dome
14 Dec 2001	2452257.85944	IC 348	<i>H</i>	20	48	960	1.262	1.81	17.69	sky
14 Dec 2001	2452257.88446	IC 348	<i>J</i>	20	46	920	1.414	1.87	17.70	sky
17 Dec 2001	2452260.81462	Off 1	<i>K</i>	30	30	900	1.112	2.10	16.97	dome
08 Feb 2002	2452313.60532	IC 348	<i>K<sub>s</sub></i>	60	16	960	1.007	1.48	17.72	dome
08 Feb 2002	2452313.62027	IC 348	<i>H</i>	60	14	840	1.020	1.49	18.04	sky
08 Feb 2002	2452313.68697	IC 348	<i>J</i>	60	24	1440	1.176	1.67	18.82	sky
11 Feb 2002	2452316.58424	Off 2	<i>K<sub>s</sub></i>	60	16	960	1.001	1.59	17.74	dome

Table 2. Comparison of Photometry to 2MASS Catalog.

Date	Target	Passband	Magnitude <sup>(a)</sup> Range	Number of Matches	Median <sup>(b)</sup> Offset	1 $\sigma$ <sup>(c)</sup> Scatter
14 Dec 2001	IC 348	<i>K</i>	11.00 – 13.75	280	0.075	0.051
14 Dec 2001	IC 348	<i>H</i>	11.00 – 14.50	345	0.049	0.053
14 Dec 2001	IC 348	<i>J</i>	11.00 – 15.50	343	0.050	0.067
17 Dec 2001	Off 1	<i>K</i>	11.00 – 13.75	103	0.073	0.033
08 Feb 2002	IC 348	<i>K<sub>s</sub></i>	11.75 – 13.75	210	0.079	0.078
08 Feb 2002	IC 348	<i>H</i>	12.00 – 14.50	267	0.086	0.066
08 Feb 2002	IC 348	<i>J</i>	12.00 – 15.50	334	0.085	0.068
11 Feb 2002	Off 2	<i>K<sub>s</sub></i>	11.75 – 13.75	98	0.077	0.078

<sup>(a)</sup>For the magnitude range compared for the FLAMINGOS and 2MASS photometry of IC 348, the bright limit depended upon the source saturation in the FLAMINGOS images while the faint limit depended upon the increase in the RMS noise of the 2MASS data with magnitude.

<sup>(b)</sup> Median Offset = 2MASS - FLAMINGOS<sub>absolute</sub>.

<sup>(c)</sup> Scatter measured after secondary offset removed.

Table 3. IC 348 Power-Law IMFs derived from Model KLFs

Cluster Region	$N_\Gamma$ ( <sup>a</sup> )	$m_K$ Limit	$M/M_\odot$ <sup>(b)</sup> Limit	$\chi^2$ Prob.	IMF Parameters <sup>(c)</sup>									
					$\Gamma_1$	$1\sigma$	$m_1$	$1\sigma$	$\Gamma_2$	$1\sigma$	$m_2$	$1\sigma$	$\Gamma_3$	$1\sigma$
cluster	3	14.0	0.040	0.70	-1.49	0.30	0.79	0.25	-0.19	0.18	0.089	0.02	+1.75	0.53
cluster	3	15.0	0.025	0.63	-1.53	0.28	0.83	0.23	-0.23	0.14	0.086	0.01	+2.28	0.22
cluster	3	16.5	$\sim 0.01$	$< 0.01$	...	...	...	...	...	...	...	...	...	...
core	2	14.0	0.040	0.93	-1.43	0.38	0.56	0.18	+0.43	0.25	...	...	...	...
core	2	15.0	0.025	0.83	-1.37	0.35	0.47	0.13	+0.59	0.17	...	...	...	...
core	2	16.5	$\sim 0.01$	0.37	-1.47	0.38	0.61	0.19	+0.32	0.19	...	...	...	...
halo	2	14.0	0.040	0.76	-0.72	0.14	0.10	0.02	+1.98	0.46	...	...	...	...
halo	2	15.0	0.025	0.41	-0.75	0.16	0.10	0.01	+2.25	0.26	...	...	...	...
halo	2	16.5	$\sim 0.01$	$< 0.01$	...	...	...	...	...	...	...	...	...	...
halo	3	14.0	0.040	0.81	-1.23	0.39	0.83	0.28	-0.55	0.14	0.093	0.01	+1.89	0.45
halo	3	15.0	0.025	0.40	-1.25	0.39	0.82	0.29	-0.53	0.14	0.092	0.01	+2.20	0.27
halo	3	16.5	$\sim 0.01$	$< 0.01$	...	...	...	...	...	...	...	...	...	...
Trap	3	...	0.025	0.99	-1.21	0.18	0.60	0.16	-0.15	0.17	0.120	0.04	+0.73	0.20

<sup>(a)</sup>Number of power-laws,  $\Gamma_i$ , used in the underlying IMF of the model KLFs.

<sup>(b)</sup>Conversion of the  $m_{K,limit}$  to  $M/M_\odot$  using the 2e6 Myr DM97 isochrone. For  $m_{K,limit} = 16.5$ , we converted to mass using the Burrows et al. (1997) and Baraffe et al. (2002) evolutionary models.

<sup>(c)</sup>Units of IMF parameters:  $\Gamma_i$  are slopes for an IMF defined as the number of stars per unit  $\log(M/M_\odot)$ ;  $m_j$  are mass breaks given in units of linear solar mass ( $M/M_\odot$ ).

Note. —  $\chi^2$  probability calculated for best fit model KLF over the range from  $m_K = 8 - m_{K,limit}$ . Average IMF parameters calculated within the 0.35 confidence contour.

Fig. 1.— FLAMINGOS  $JHK_s$  infrared color composite image of IC 348. For orientation, north is up while east is left and the field of view is  $20.5 \times 20.5'$ . The bright blue star to the north by northwest is  $\alpha$  Persi. The cluster's interface with the Perseus Molecular Cloud is clearly outlined by a series of nebular features and enshrouded or heavily reddened sources along the southern edge of the image. The series of blue-green-red sources to the south by southwest of the cluster center is the asteroid 545 Messalina. Individual images were obtained 08 February 2002 with a resolution of  $0.6''/\text{pixel}$  and a typical seeing of  $1.6''$ .

Fig. 2.— Infrared color-magnitude diagrams for sources detected in the IC 348 FLAMINGOS wide-field images. No radial or photometric criteria have been applied to the sources in these diagrams. The locations of the sources in these diagrams are compared to the location of the D'Antona & Mazzitelli (1997) and Baraffe et al. (1998) pre-main sequence isochrones for 2 and 5 Myr at 320 pc. Reddening vectors (Cohen et al. 1981) with length  $A_V = 7$  are drawn for 1.4, 0.08 and  $0.02 M_\odot$  PMS objects at the cluster's mean age. A)  $J-H/H$  color-magnitude diagram containing 1534 sources (82% of total); B)  $H-K/K$  color-magnitude diagram containing 1739 sources (93% of total).

Fig. 3.— Infrared color-color diagram for sources in the IC 348 FLAMINGOS region with  $m_K < 15$ . This diagram has not been filtered by photometric error and includes 97% (563/580) of the sources brighter than this  $K$  magnitude limit. This observed color distribution is compared to the intrinsic colors of field dwarfs (O-M9, Bessell & Brett (1988); Kirkpatrick et al. (2000, , where the Bessell & Brett colors were shifted by zeropoint offsets to the 2MASS system using the relations derived by Carpenter 2001))), classical T-Tauri stars with optically thick disks (Meyer, Calvet & Hillenbrand 1997), and giants.  $\sim 12\%$  of the sources display excess infrared emission in this diagram. A reddening vector of length  $A_V = 7$  illustrates the modest reddening seen by the majority of the cluster.

Fig. 4.— Radial Profile of the IC 348 Cluster. Surface density (in stars per square degree) is measured in circular annuli, centering on the location of the LL95 sub-group IC348a. Profiles are calculated using annuli of equal area (histogram with bins of decreasing width) and annuli with equal radial steps (heavy solid line with error bars). The width of the first annuli was  $R_0 = 1.75'$ . Profiles are compared to the unreddened background surface density (lightly shaded band; width =  $2 \times$  the  $1\sigma$  deviation of background, see text) and the background surface density reddened by  $A_V \sim 4$ . Also shown: the division of cluster into sub-regions (vertical dashed lines, see text); a  $1/r$  profile fit to the entire cluster region (dot-dashed line;  $\chi^2 \sim 4.9 \times 10^{-4}$ ); and a King profile fit to the cluster core (dotted line;  $r_{core} = 0.25\text{pc}$ ;  $\chi^2 \sim 1$ ). Note(s): bins with  $R \geq 10.33'$  have been geometrically corrected to account for the survey boundaries and the conversion from angular to physical scale (upper x-axis) is calculated for a distance of 320 pc.

Fig. 5.— Spatial distribution and surface density profile of IC 348 sources. A) Locations of sources in different magnitude ranges are shown in an equatorial tangent projection of the wide-field FLAMINGOS IC 348 region. Large filled stars correspond to sources with spectral types A5 and earlier including the B0III giant  $\alpha$  Persi. Large filled circles correspond to sources  $m_K < 10$ , smaller filled circles,  $10 < m_K < 15$ , and small open circles,  $m_K > 15$ . B) The surface density of IC 348 sources is shown filtered by a Nyquist sampled box (width =  $200''$ , see upper left). Only sources  $m_K < 15$  are used and contours are given as multiples of the field star surface density derived by reddening the off-field by  $A_V \sim 4.0$  or the same field star surface

density shown as the darkly shaded band in Figure 4 (i.e., 2305 stars/sq. deg). In this figure, filled circles correspond to sources displaying infrared excess in Figure 3. The  $R < 5'$  and  $R = 10.33'$  boundaries of the cluster sub-regions are shown as concentric circles.

Fig. 6.— Extinction Maps of the IC 348 FLAMINGOS Region. Individual source  $A_V$  estimates derived in Section 2.4.1 are converted to an extinction map using a Nyquist sampled box filter (width =  $200''$ ; see upper left; same as previous figure). Contours are in steps of  $A_V = 1$  from  $A_V = 1$  to 20; we label the  $A_V = 2, 5, 10$  contours. Left hand panel:  $A_V$  map derived from the bright, likely cluster members; Right hand panel:  $A_V$  map of the extinction seen by the fainter, likely background stars. See text for sample selection and explanation of reddening estimates.

Fig. 7.— Observed distribution of  $H - K$  color and derived  $A_V$  distribution for sources in IC 348. Panels (A) and (B): the fractional distribution of  $H - K$  color divided by sub-region. Panels (C) and (D): the probability distributions of  $A_V$  derived from de-reddening sources in the  $(H - K)/(J - H)$  color-color diagram. In all panels, the distributions are divided into the results from magnitude limited “bright” and “faint” samples. See text for sample selection and explanation of de-reddening.

Fig. 8.— Raw  $K$  band luminosity functions of IC 348 separated by sub-region. The KLFs are scaled to stars per square degree and are compared to the observed field star KLF derived by combining the two off-cluster fields. Both the cluster core and halo sub-regions appear to dominate the un-reddened off-field counts for  $m_K < 15$ . Error bars are  $1\sigma$  counting statistics.

Fig. 9.— Field star correction to the raw IC 348 sub-region KLFs. Panels (A) and (B) compare the raw sub-region KLFs to the observed field star KLF convolved with the  $A_V$  distributions for background stars derived in Section 2.4 and displayed in Figure 7. The reddening field star KLF(s) are scaled only the area of the cluster sub-region and subtracted to yield the differential KLFs displayed in panels (C) and (D). The differential KLFs are significant for  $m_K \leq 16.5$ , below which we over-estimate the field star correction. Error bars are the square root of the sum of the observed counts and the predicted field star counts for each bin.

Fig. 10.— Differential IC 348 KLFs by region. A) Comparison of the differential IC 348 KLFs for the two cluster sub-regions. B) Sum of sub-region differential KLFs into the composite IC 348 KLF. Panel B compares the sum of the sub-region differential KLFs from two different background corrections. The “Red” correction is the field star KLF reddened by the EPDF for the background stars; the “Blue” correction is the field star KLF reddened by the EPDF for the bright cluster stars.

Fig. 11.— The Star Formation History of IC 348. The star formation history of IC 348 from Herbig (1998) is compared to that SFH used in our model luminosity function algorithm. The Herbig SFH is the merger of the ages derived for stars with and without detectable  $H\alpha$  emission using the de-reddened optical color-magnitude diagram. The SFH assumed for our models has a mean age,  $\tau = 2.0$  Myr with constant star formation from 0.5 to 3.5 Myr ago.

Fig. 12.— Comparison of theoretical mass - apparent  $K$  magnitude relations relevant for IC 348. Mass- $K$  magnitude relations from two different sets of theoretical evolutionary models and having different ages and distances are compared to illustrate the sensitivity of our method to assumptions about cluster distance and age. Mass- $K$  magnitude relations from D’Antona & Mazzitelli (1997) are shown at  $\tau = 2, 3$  and 10 Myr for a distance of 320 pc and at  $\tau = 3$  Myr for a distance of 260 pc. Mass- $K$  magnitude relations from the Baraffe et al. (1998) tracks are also compared at 2 and 10 Myr at a distance of 320pc. For all of these comparisons, the PMS tracks were converted to observables using a single tabulation of bolometric corrections.

Fig. 13.— Fits of model KLFs to the composite IC 348 Cluster KLF and resulting cluster IMFs. The left hand panel compares the best fit model KLFs to the composite differential IC 348 KLF. The right hand panel compares the IMFs of these model KLFs to the IMF derived for the Trapezium cluster by Muench et al. (2002), although the Trapezium is only the  $R < 0.3$  pc core of the larger Orion Nebula Cluster (Hillenbrand 1997). Model KLFs and IMFs for IC 348 have corresponding symbols.

Fig. 14.— Best fit Model KLFs and underlying IMFs for the IC 348 core/halo sub-regions. Left hand panels display model KLFs best fit to the differential IC 348 KLFs of each sub-region (upper: core; lower: halo). The best fit model KLFs are normalized to the observations over a range from  $m_K = 8-14$ , corresponding to a mass range from  $2.5$  to  $0.04M_{\odot}$ . Right hand panels display the underlying two and three power-law IMFs corresponding to the specific model KLFs (by symbol). Derived IMF parameters are listed in Table 3.

Fig. 15.— Comparison of the IC 348 and Trapezium  $K$  band Luminosity Functions. Panel (A) compares the  $K$  band LFs of IC 348 and the Trapezium, shifted to absolute magnitudes. No reddening corrections have been included but the Trapezium KLF has been scaled to contain the same number of stars as IC 348. Panel (B) compares the IC 348 differential KLF to two model KLFs representing the Trapezium evolved to the age of IC 348. The models use the star forming history and reddening for IC 348 but substitute the Trapezium IMF derived in MLLA02 and use two different sets of PMS tracks (D’Antona & Mazzitelli 1997; Burrows et al. 1997, DM97 and Bur97). This illustrates the predicted location and size of the secondary KLF peak of the Trapezium were this cluster the age of IC 348.

Fig. 16.— Comparison of the Core and Halo Sub-Region IMFs for IC 348. Shown are Monte Carlo simulations of the derived IMFs for the IC 348 sub-regions and calculated for a sample of 150 stars. Error bars, calculated as the  $1\sigma$  variation in each IMF bin from 100 iterations, are shown every 0.3 dex in log mass for clarity. These sub-region IMFs are also compared to two published derivations of the IC 348a sub-cluster derived by Najita, Tiede, & Carr (2000) using NICMOS narrow band imaging and by Luhman et al. (2000) using a merger of optical and infrared spectra with infrared colors. Both sample somewhat smaller areas and contain fewer sources than the cluster “core” defined here and were scaled up in number for comparison. Error bars for the NTC00 study taken directly from that work.

*Figure 1*

1

3 Color FLAMINGOS Image of IC 348.  
Figure separately included as jpg (to make smaller).

Figure 2a

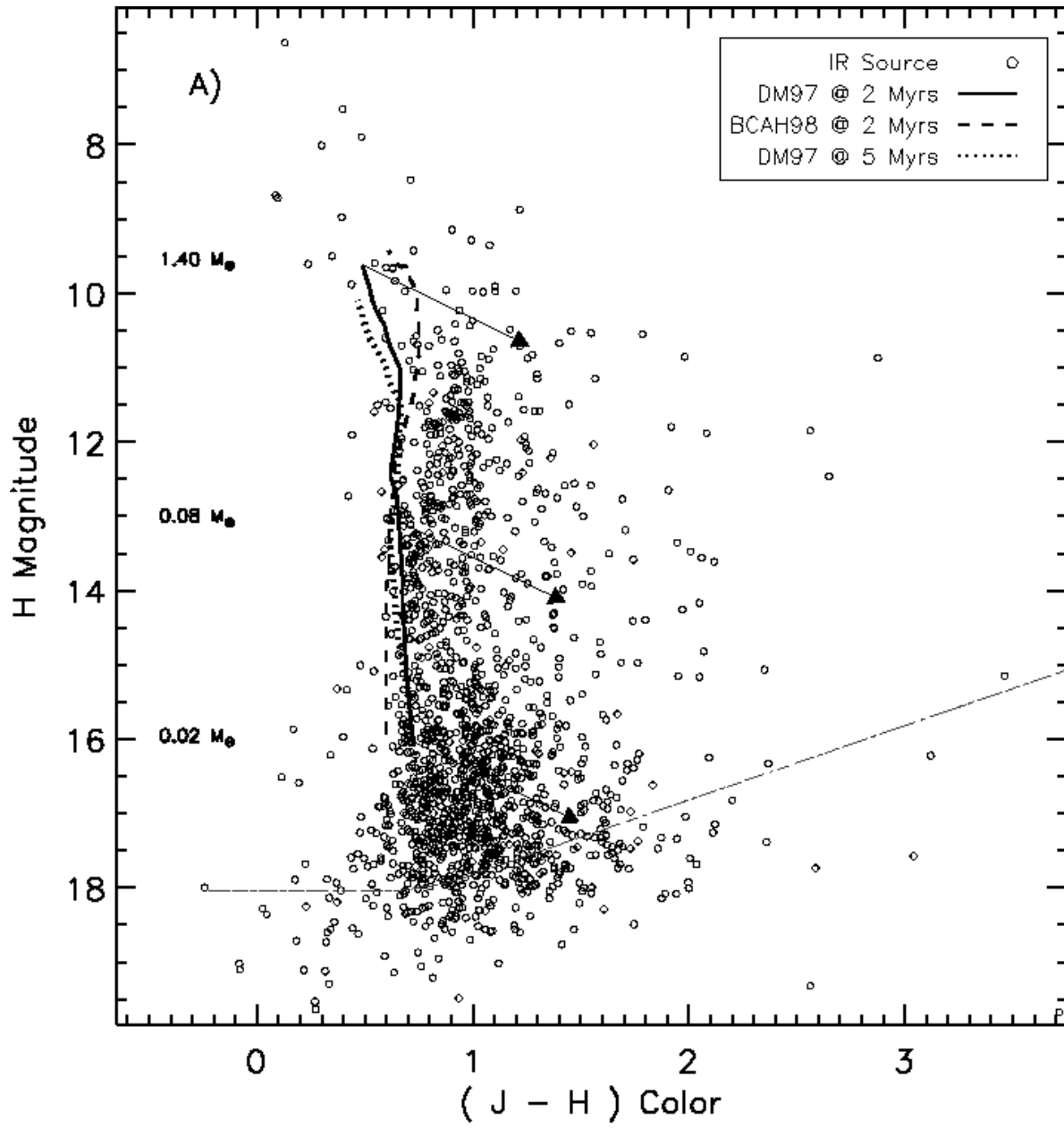


Figure 2b

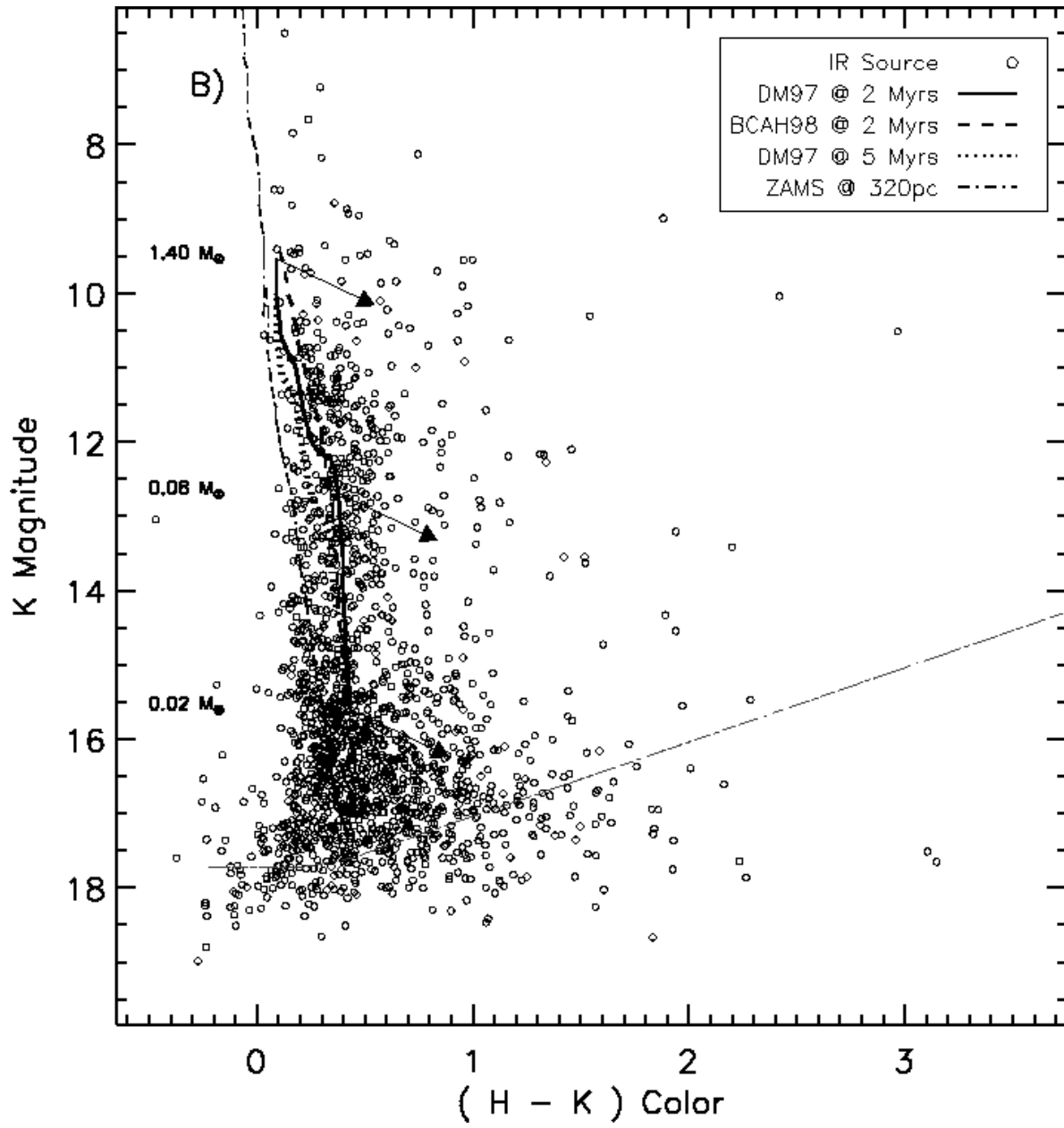


Figure 3

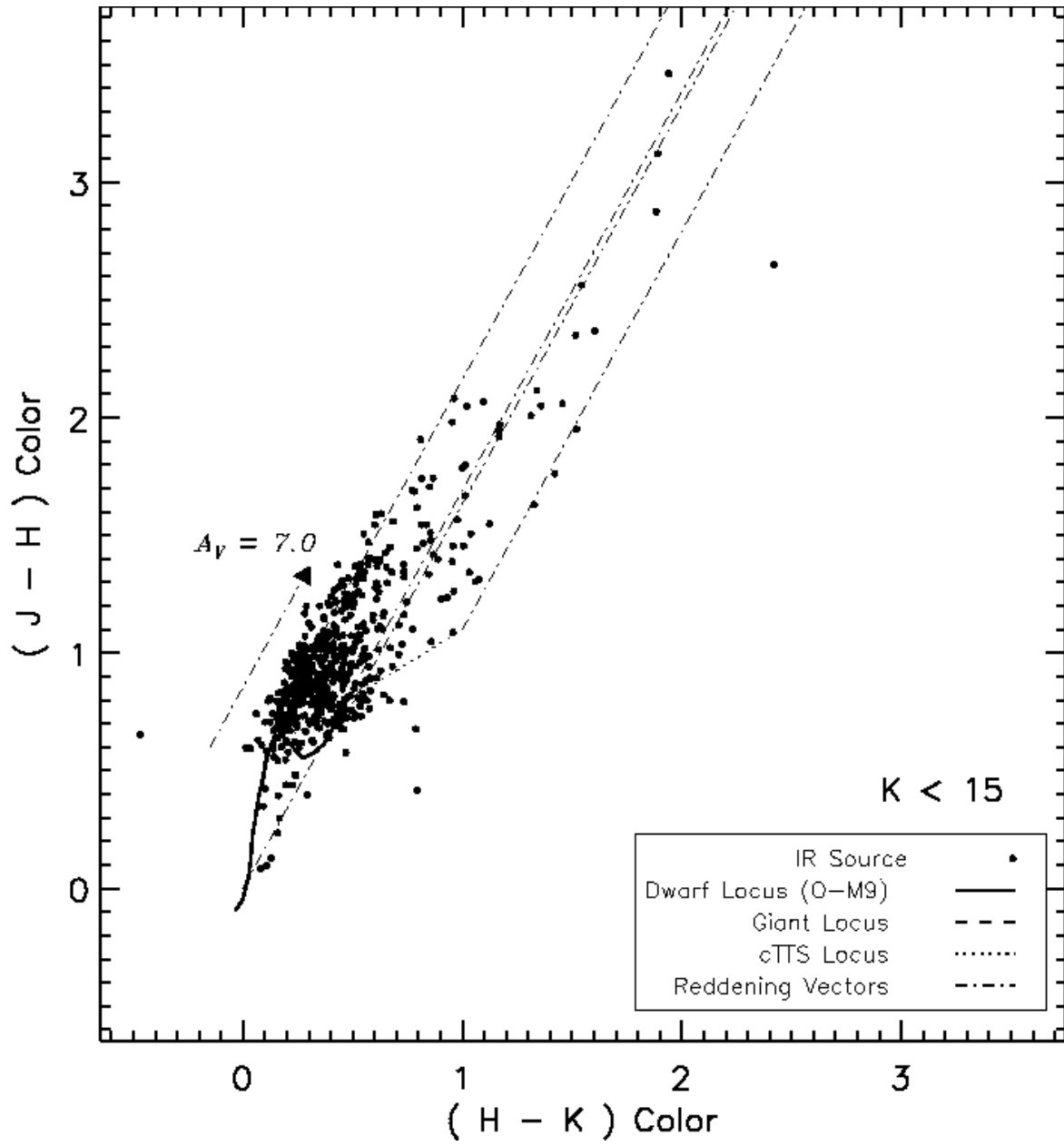


Figure 4

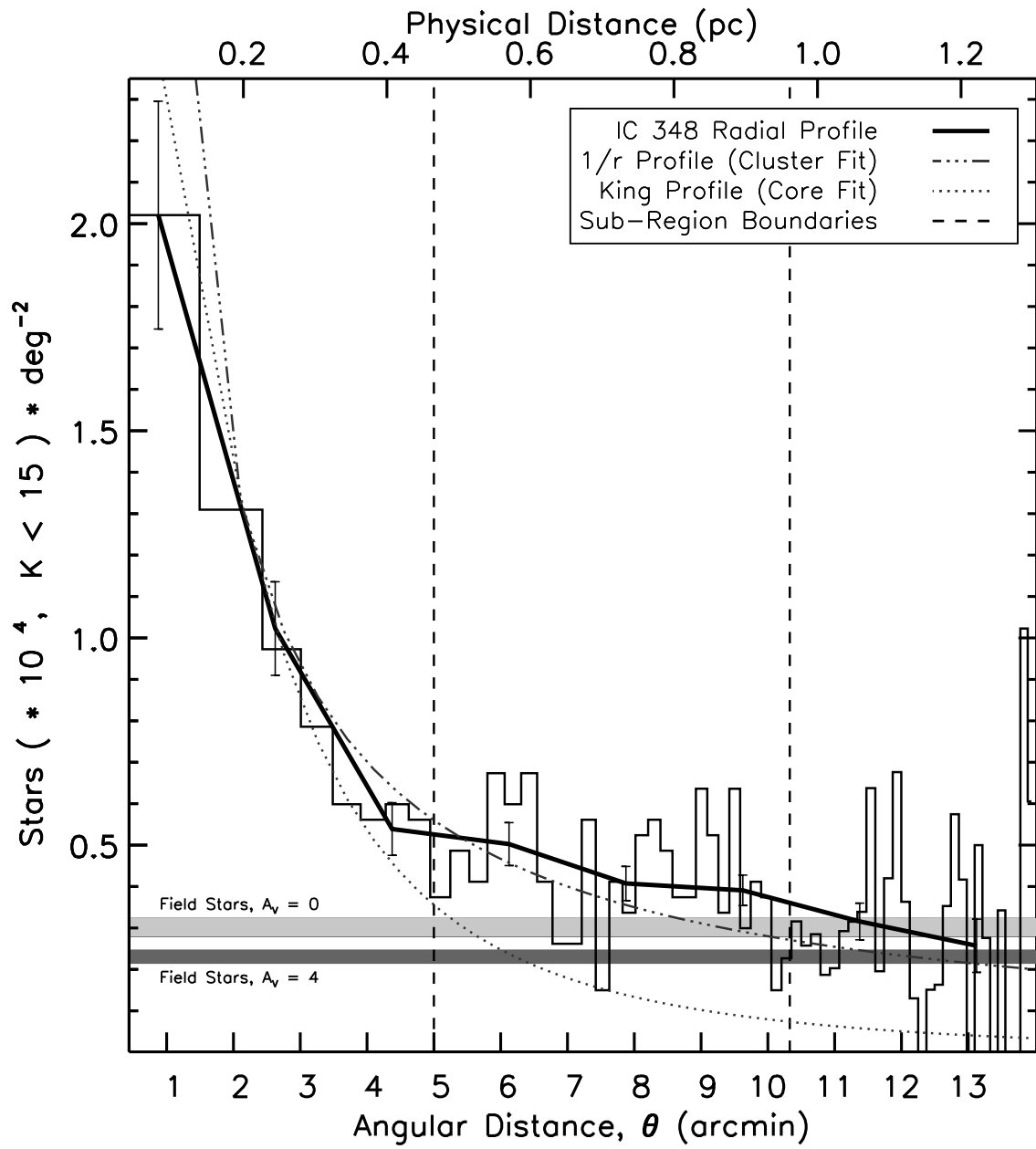


Figure 5a

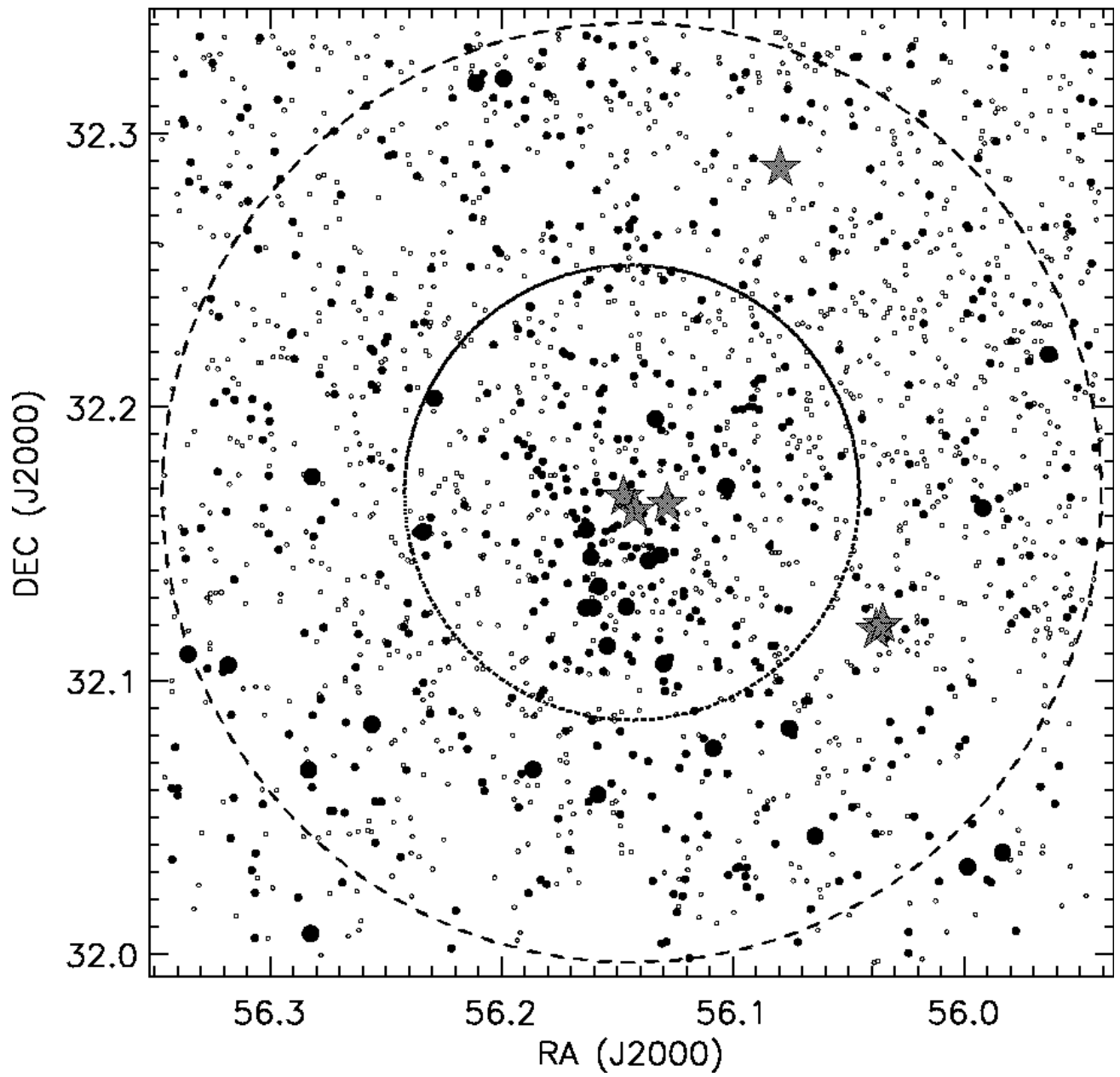


Figure 5b

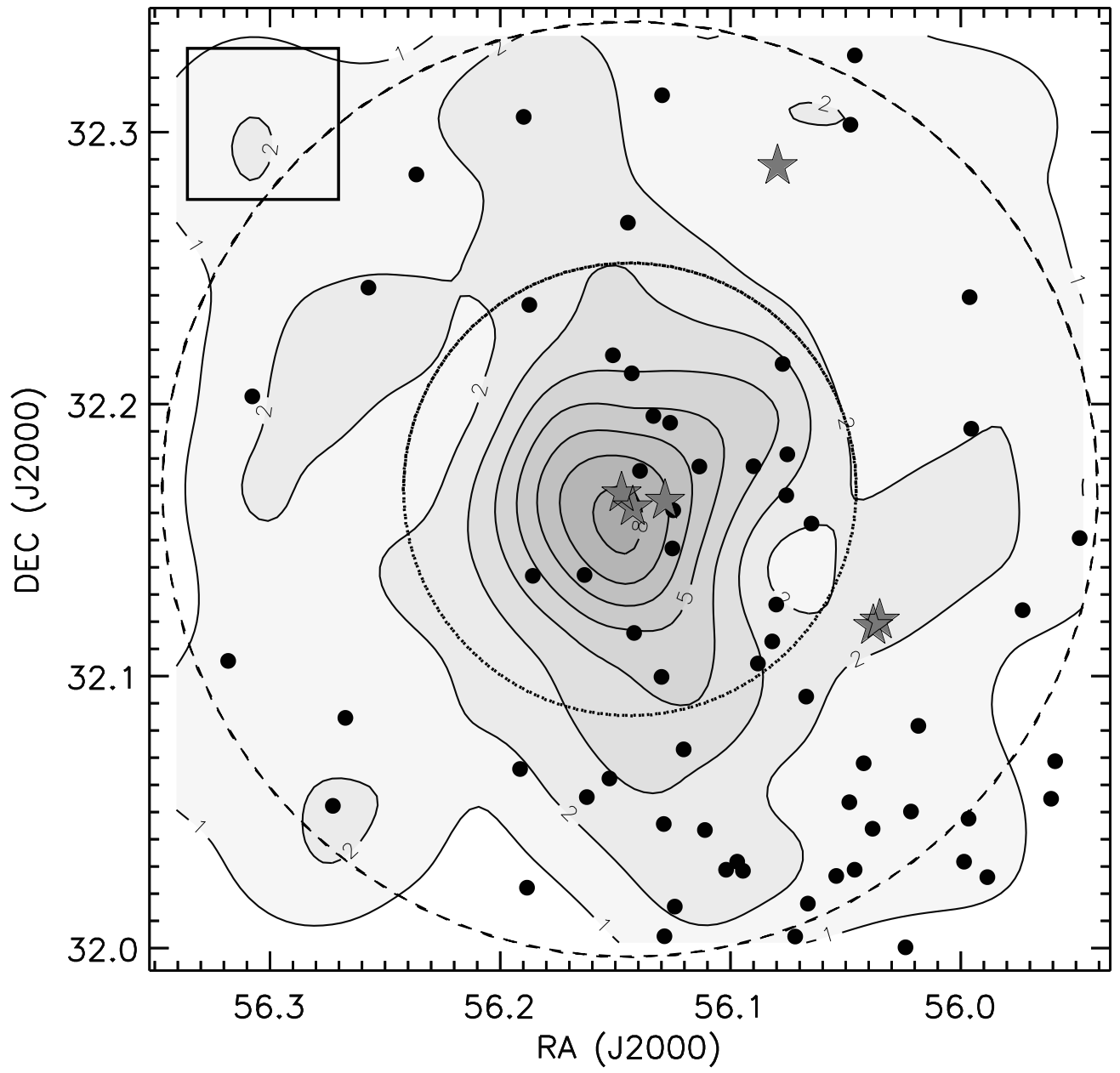


Figure 6a

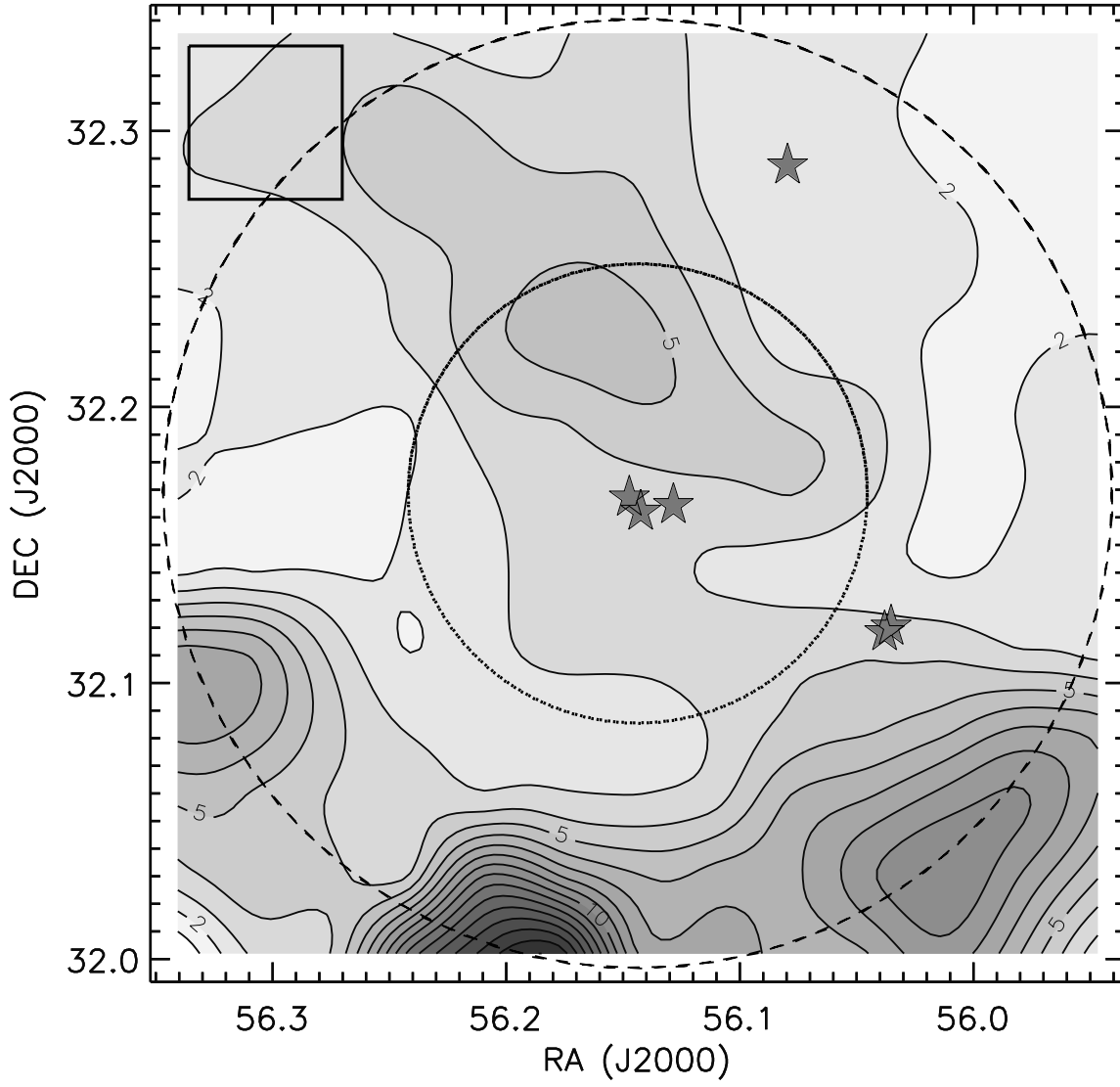


Figure 6b

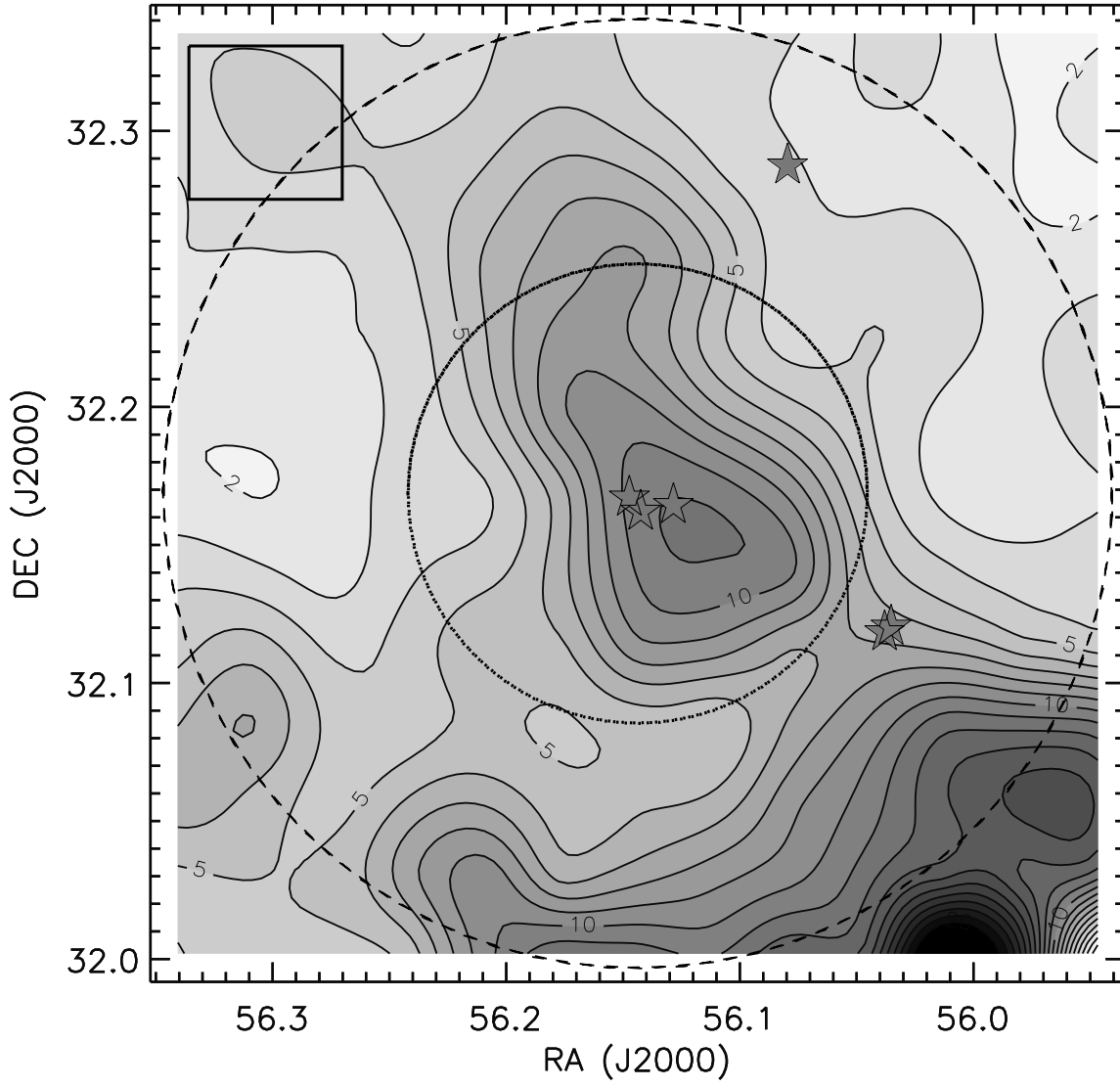


Figure 7

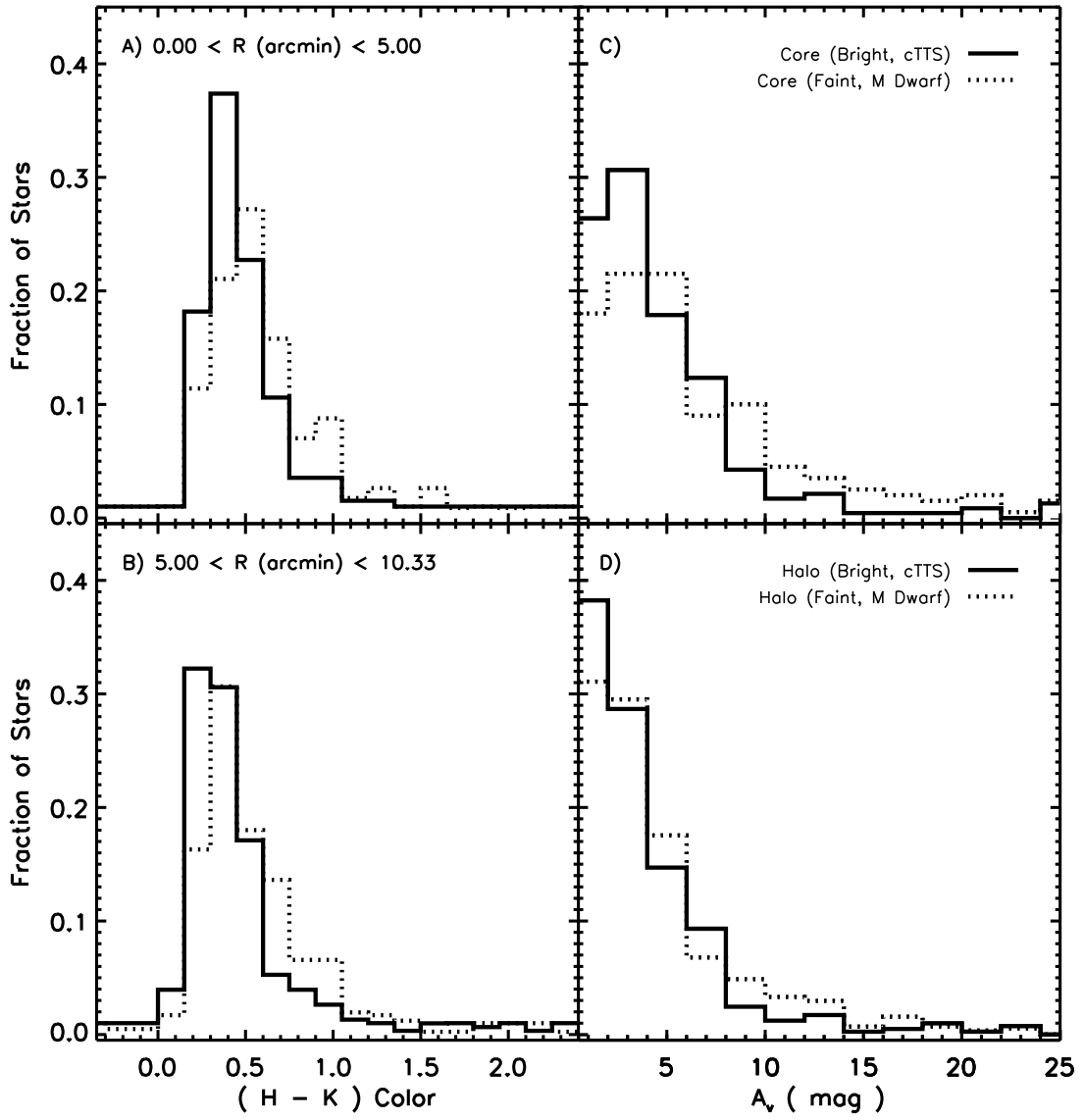
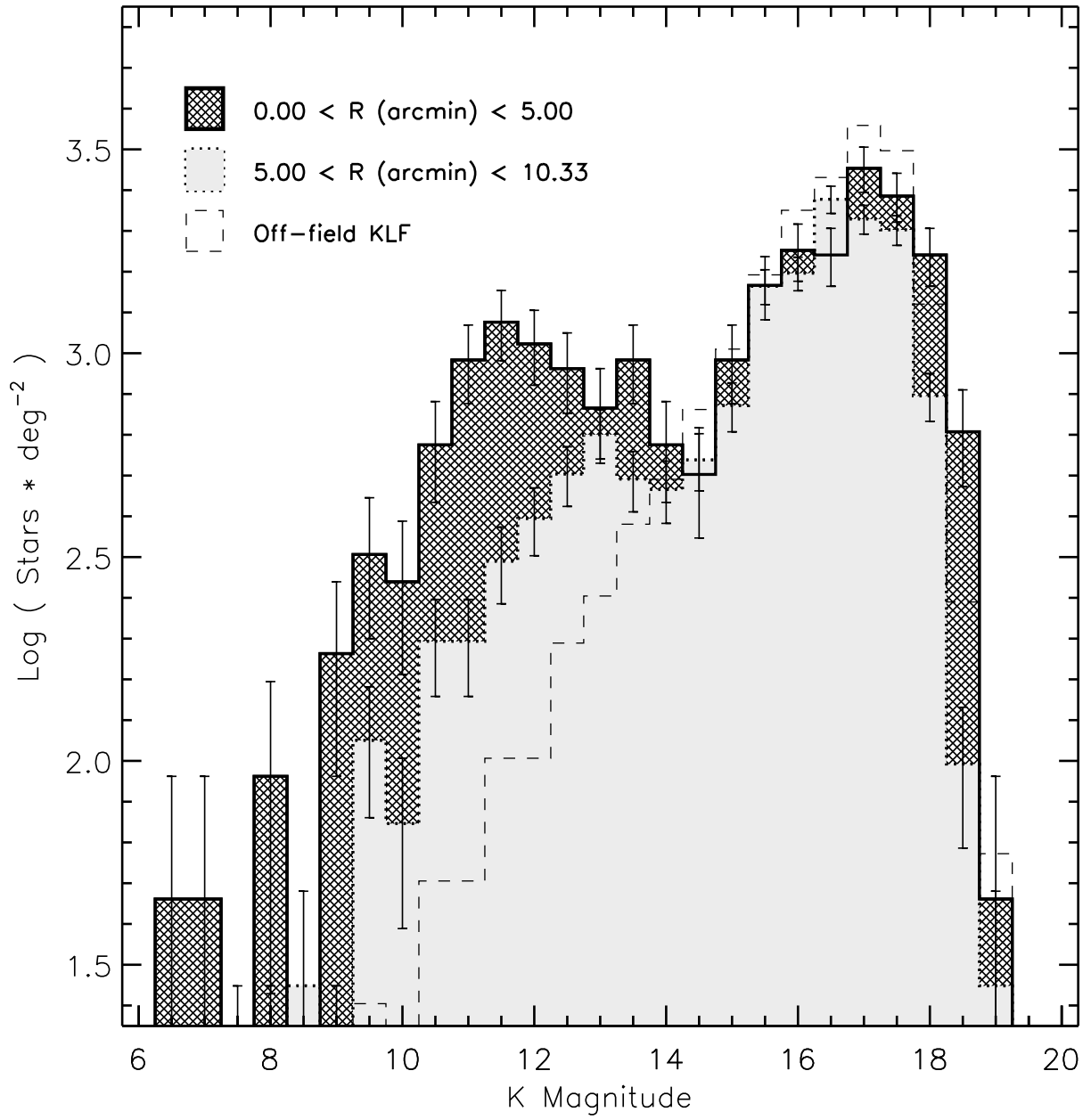


Figure 8



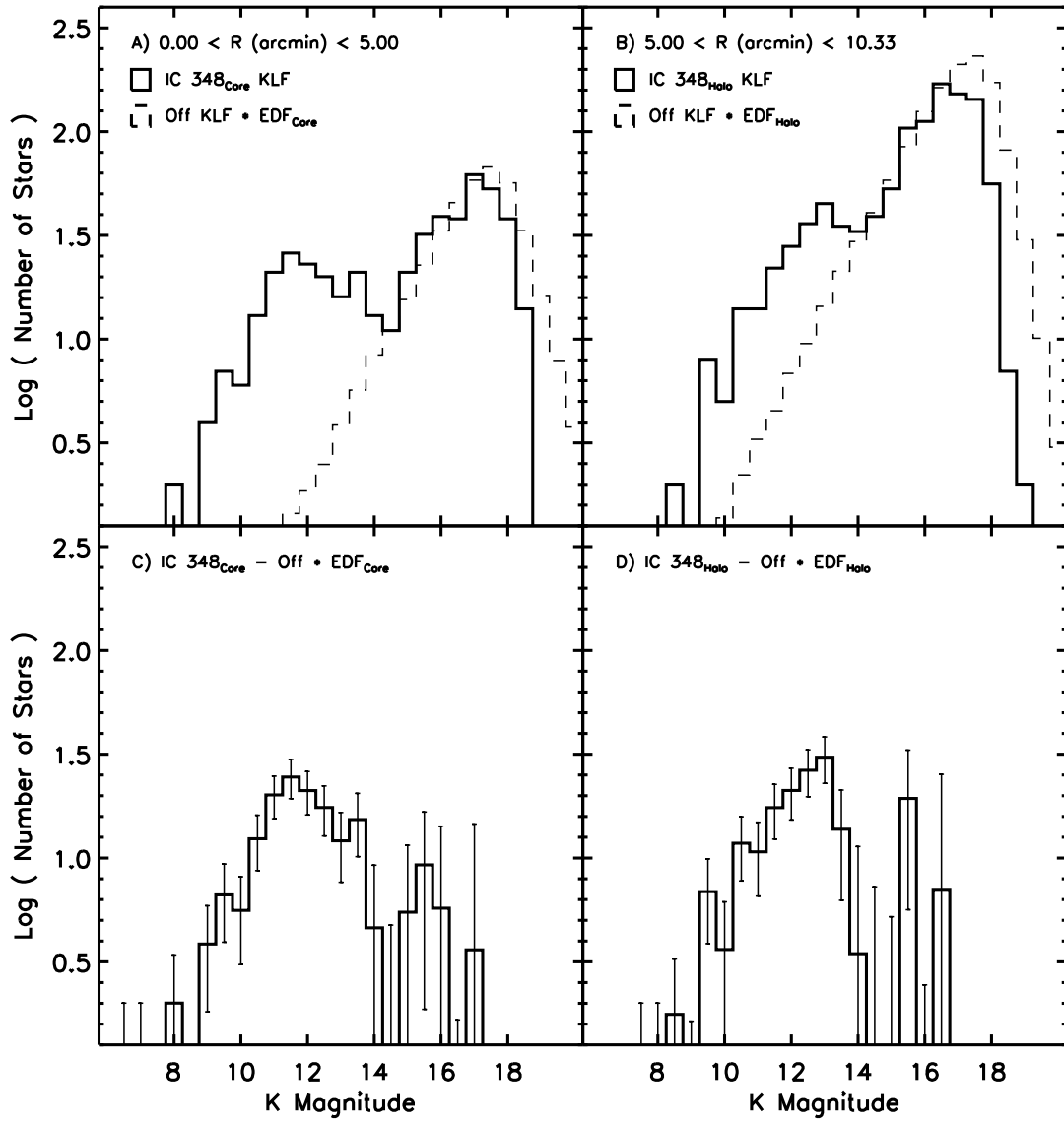


Figure 10

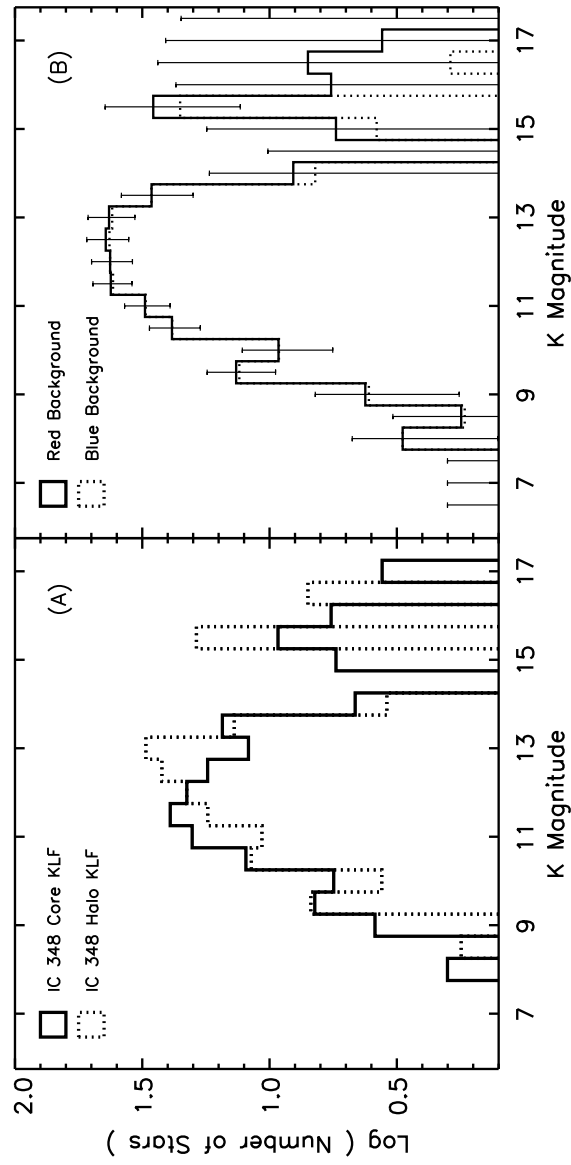


Figure 11

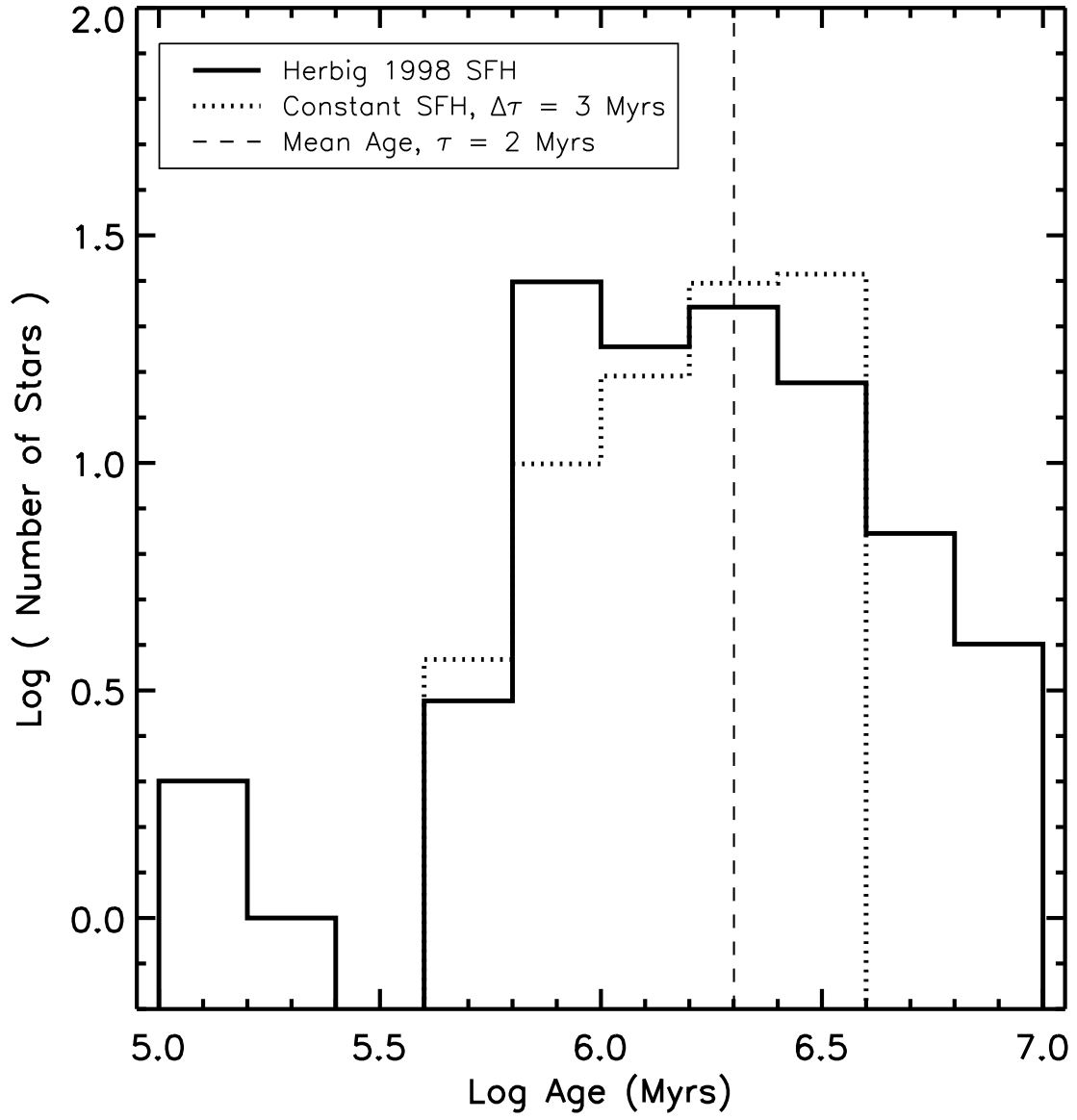
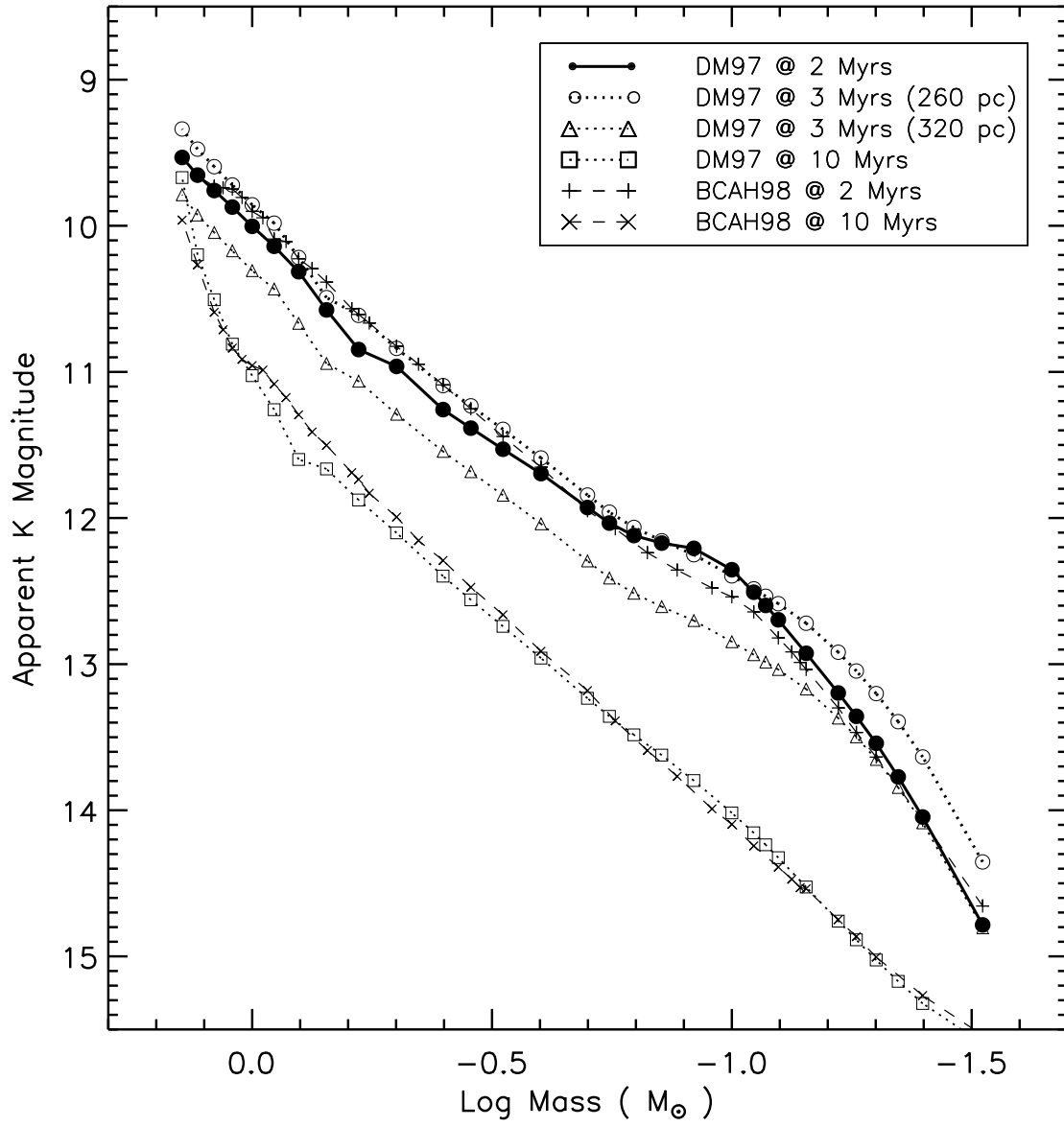


Figure 12



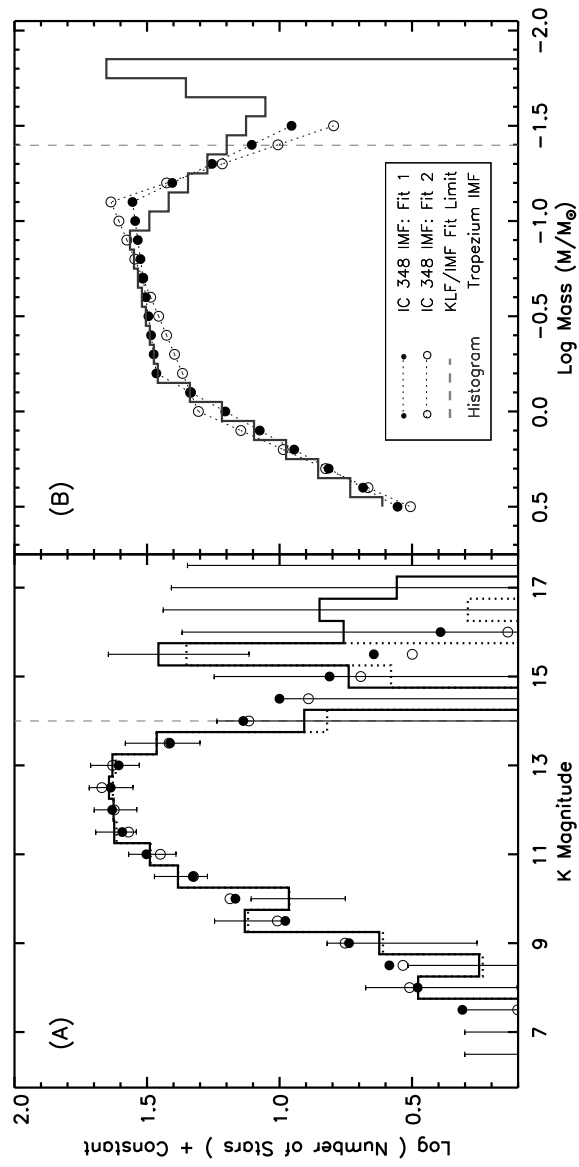
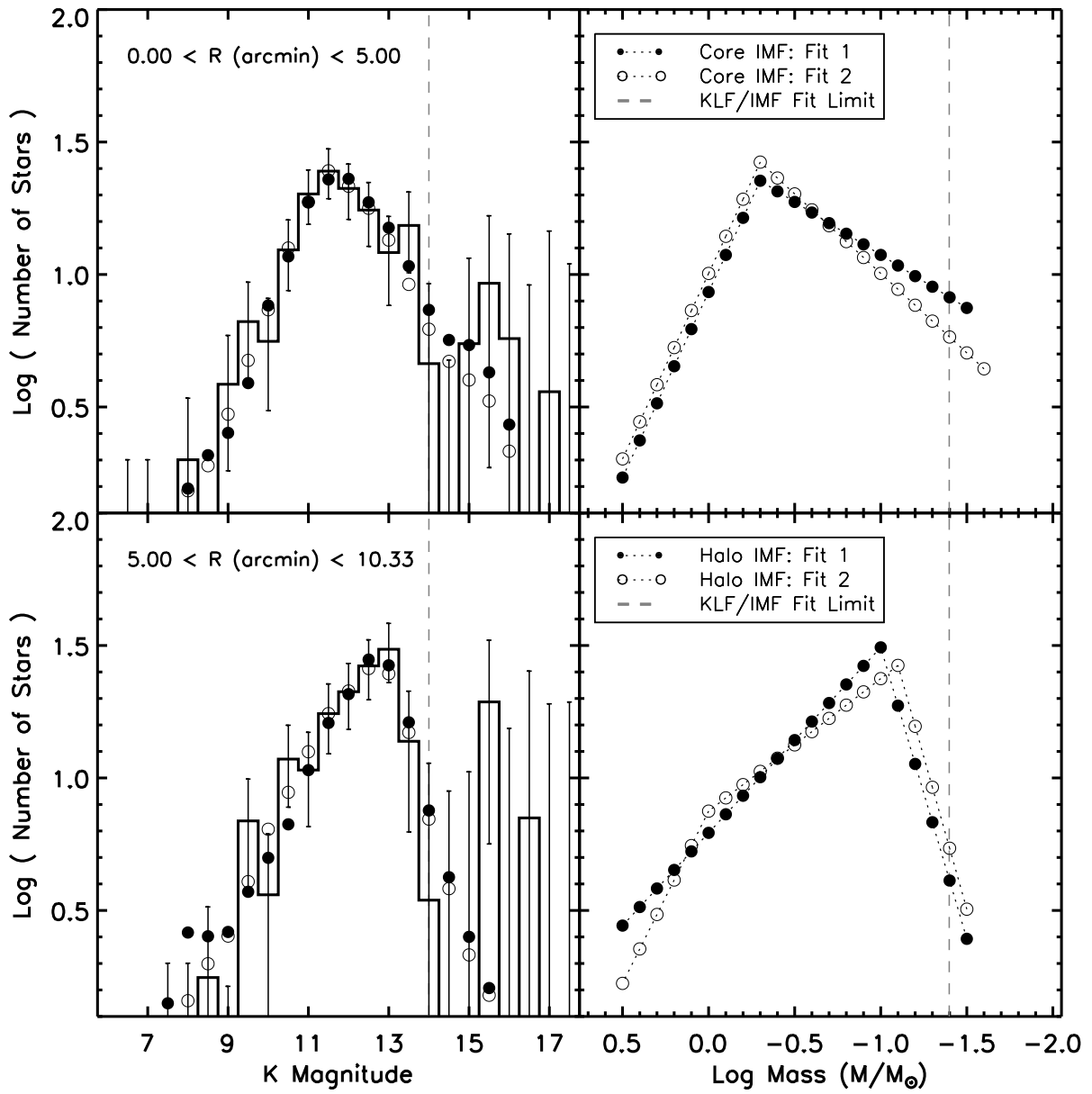
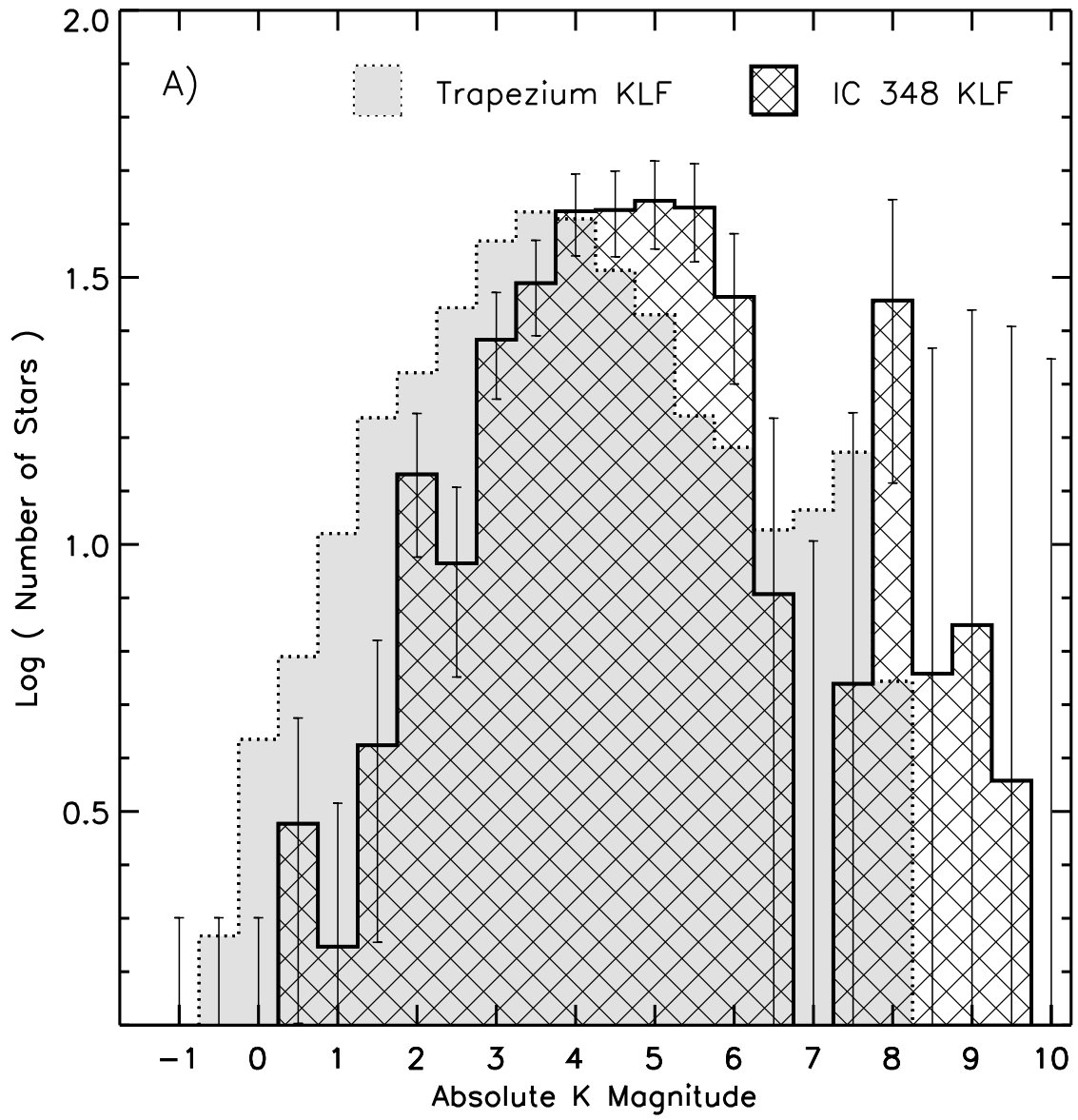
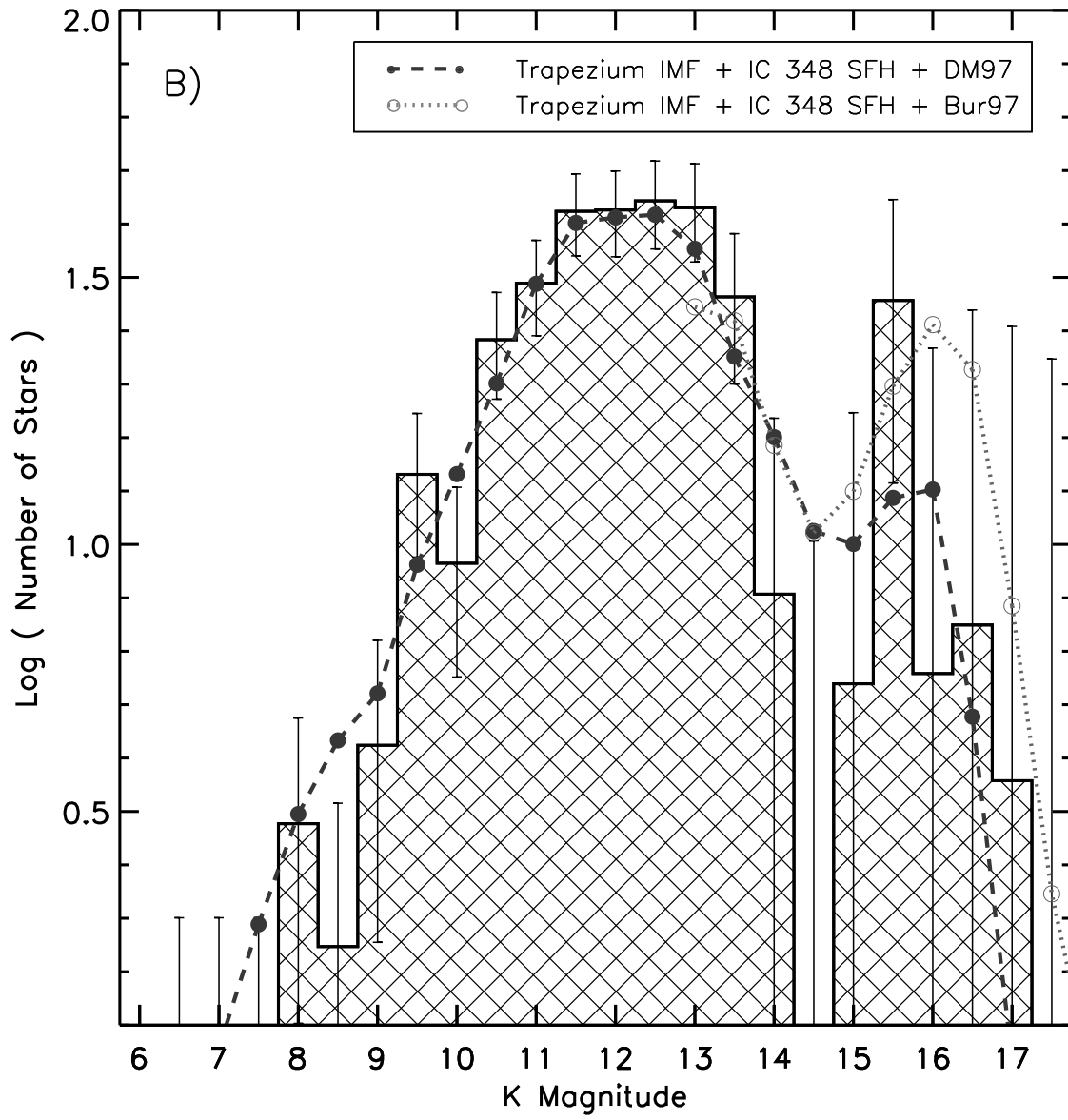
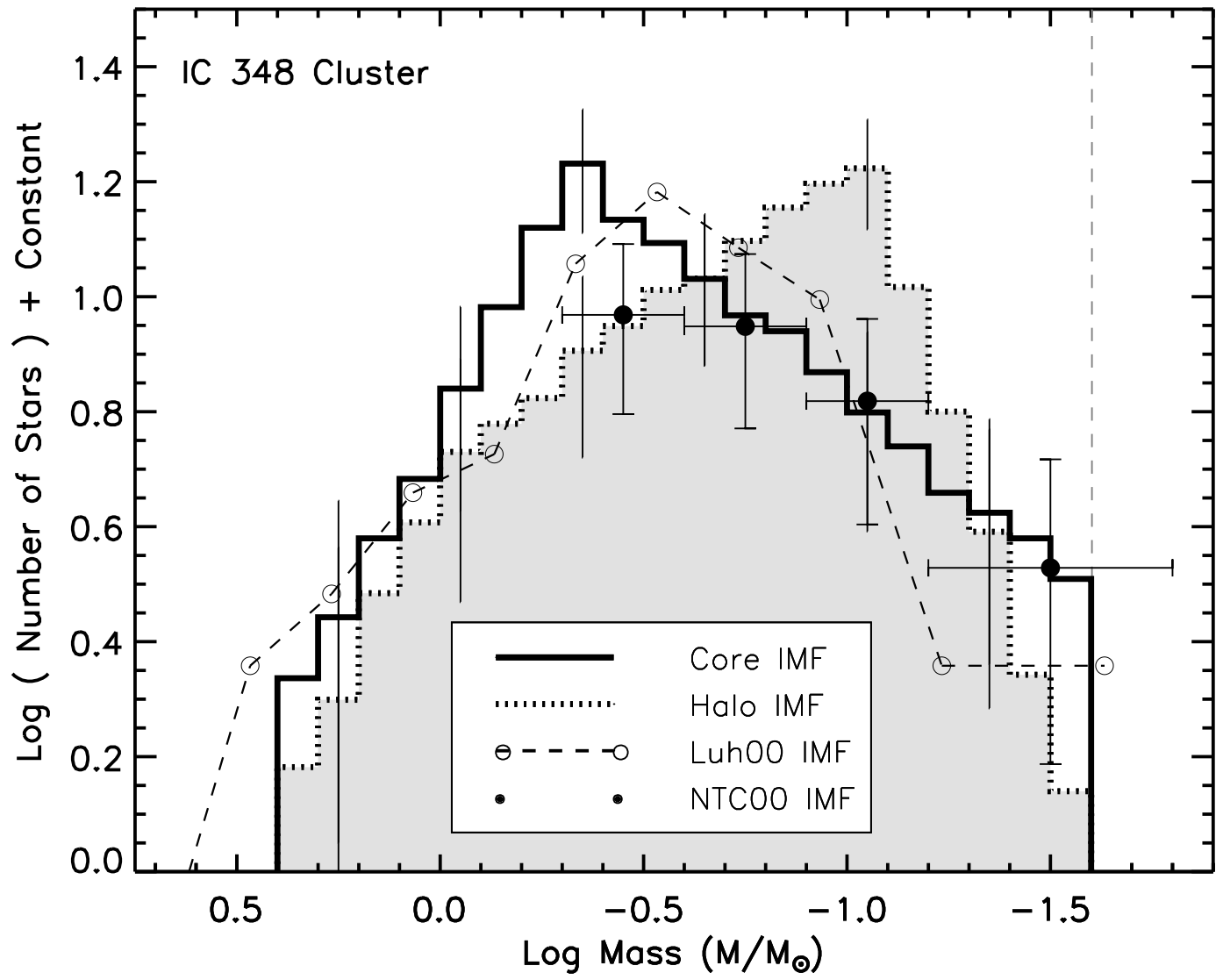


Figure 14









This figure "figure01.jpg" is available in "jpg" format from:

<http://arxiv.org/ps/astro-ph/0301276v1>